Centrifuge-aided Micromolding and Sintering of Micron- and Submicron-sized Ceramic Features

Hongfei Ju

Thesis submitted to the faculty of the Virginia Polytechnic Institute and State University in partial fulfillment of the requirements for the degree of

Masters of Science

In

Materials Science and Engineering

Peizhen Lu, Chair

Alexander O. Aning

Carolina Tallon Galdeano

11/29/2017

Blacksburg, VA

Centrifuge-aided Micromolding and Sintering of Micron- and Submicron-sized Ceramic Features

Hongfei Ju

Abstract

Microfabrication of ceramic features has become a critical issue in realizing the miniaturization of devices. Micromolding and sintering play critical roles in fabricating micron- and submicron-sized ceramic features using nanoparticles.

Developed from soft lithography, replica molding has been proven a good method to prepare micron- and submicron-sized features. However, the fidelity of the features can be compromised by incomplete feature cavity filling and feature shrinkage during the forming process. In this study, centrifuge-aided micromolding is developed to prepare micron- and submicron-sized ZnO features. By introducing a centrifugal force, the shear-thinning behavior of the suspensions is utilized, and the cavity filling process and the diffusion of trapped air out of the features are accelerated. The drying shrinkage is decreased by increasing the density of the wet nanoparticle packing from the centrifugal process. The centrifugal force improves the fidelity of all the designed features. ZnO ridges from 0.4 μm to 2 μm size and rods of 1.6 μm size are prepared successfully. The wide applicability of this strategy has been demonstrated by preparing ZrO_2 features via the same method.

Sintering process has a significant influence on the morphology and microstructural evolution of micron-sized ceramic features. When ceramic features decrease to much smaller sizes, such as in the micron range, the dominating sintering mechanism(s) can be different from those of the bulk at large scales. However, limited effort has been devoted to understanding the sintering behaviors. In this study, the as-prepared micron-sized ZnO ridges and rods were sintered at 950°C for different time in air atmosphere. The sintering process destructs the ZnO features via abnormal grain growth and surface roughening. Destruction prediction of features using sintering time is established based on grain growth. Feature surface roughening is further analyzed with respect to thermodynamic fundamentals.

Because of the evaporation tendency during zinc oxide sintering, sintering atmosphere has a significant influence on the sintering behavior and feature fidelity. In this study, micron-sized ZnO ridge features were sintered under air and argon atmospheres. Ridge size, line edge roughness, and grain size were characterized. Quantitative calculation of sintering behaviors

was performed in order to obtain fundamental understating of the micron-sized ZnO feature sintering. It is found that oxygen partial pressure is the deciding factor for the ridge feature evolution. ZnO evaporation and defects diffusion are responsible for the ZnO bulk and ridge sintering behavior differences.

Centrifuge-aided Micromolding and Sintering of Micron- and Submicron-sized Ceramic Features

Hongfei Ju

General Audience Abstract

In order to produce portable devices with small sizes, novel techniques are required to make small components, which is called microfabrication. Since ceramic materials are widely used in various electronic devices, microfabrication of small ceramic features has become an important issue. When ceramic nanoparticles are used as the raw material, the fabrication of ceramic features mainly consists of two processes: micromolding and sintering, which are the problems that this thesis focuses on. In the micromolding process, the loose nanoparticles are packed to form features with specific shapes. In the sintering process, the nanoparticles in as-prepared features are bonded into a coherent and dense feature.

For the micromolding process, a suspension made from the nanoparticles is poured into a mold with as-designed feature shape, and the dry feature is obtained after a drying process. In this study, the factors that will affect the shape of the features are studied. It is found that the major factors include completeness of the filling process and shrinkage during the drying process. By completing the micromolding process in a centrifugal machine, the micromolding process is accelerated, and the shrinkage during the drying process is decreased. Both the two aspects will benefit the feature quality. By using this technique, zinc oxide ridges from 0.4 μm to 2 μm size and rods of 1.6 μm size are fabricated successfully. It is also demonstrated that this technique can be applied to other ceramic materials.

 Sintering process can convert packed nanoparticles into a coherent object, which can help us to obtain dense ceramic features. However, the sintering process will cause the change in feature shape. For large size ceramic bulks, the sintering theory has been well established to explain these changes. When the size of ceramic materials decreases to very small scale, such as micron size, new sintering theory is needed to explain the change of ceramic features in the sintering process. In this study, micron-sized zinc oxide ridges and rods were sintered at $950^{o}C$ for different time. It was found that the sintering process will distort the shape of the zinc oxide features. Based on thermodynamic views, the corresponding new theory was established.

Because zinc oxide is relatively easy to evaporate during sintering, sintering atmosphere will also affect the shape of the features. In this study, micron-sized zinc oxide ridge features were sintered under air and argon atmospheres. It was found that oxygen content

was the major factor that will affect the shape change. The corresponding theory was established to explain the effect of the sintering atmosphere based on thermodynamic views.

Acknowledgements

I greatly appreciate my advisor, Prof. Dr. Kathy Lu, who contributes her guidance, time and comments to my academic research during the past two years. Thanks to cultivation for my academic and professional skills, I can complete my research target and obtain my master degree.

Thanks a lot to my committee members Dr. Alex Aning, and Dr. Carolina Tallon for their time, comments and advice. Many thanks to Dr. Kaijie Ning who provides enormous support in my academic research. Thanks to the members of my research group, Kaustubh Bawane, Donnie Erb, Kris Shen, Michelle Gervasio and Zhihao Hu, for the conversation and friendship over years. Thanks to Dr. Thomas Staley and Hesham Elmkharram for the guidance of my laboratory works. Thanks to Steve McCartney and Dr. Aijie Chen who work in the institute of Nanoscale Characterization and Fabrication Laboratory for the assistance in using scan electron microscope and focus ion beam microscope. Additional thanks go to the entire Materials Science and Engineering department staff for their administrative support. Thanks also to Dr. Richey Davis gives me the access to the centrifugal machine. I would like to thank my family for their support, patience, and confidence.

Table of Contents

List of Figures

1 Introduction

1.1 Soft lithography

In order to realize the miniaturization of devices, effective microfabrication approaches are required for components with small sizes. In recent years, many microfabrication techniques have been developed to fabricate micron-sized features, such as soft lithography,[1] photolithography [2], focus ion beam milling [3], photomasking [4], and electron beam lithography [5]. Since the 1990s, many techniques and applications based on soft lithography have been developed to fabricate micro- and nano-structures (Fig. 1.1) [6]. Since this strategy has been proved to be convenient, effective and low-cost, to date, many kinds of soft lithography techniques have been developed, such as replica molding [7, 8], decal transfer lithography [9], microtransfer molding [10, 11], nanotransfer printing [4], micromolding in capillary [12], nanoskiving [13], and solvent-assisted micromolding [14]. By using replica molding, as-designed features can be transferred to the surface of target samples directly (Fig. 1.1a), and microtransfer molding can fabricate the features on a substrate (Fig. 1.1b). By utilizing the capillary force, a faster movement of the prepolymer in the features space can be realized (Fig. 1.1c), and by introducing a wetting liquid layer, the movement of the prepolymer can be accelerated further (Fig. 1.1d). Among these techniques, replica molding has been proved the easiest and most efficient way to create simple features.
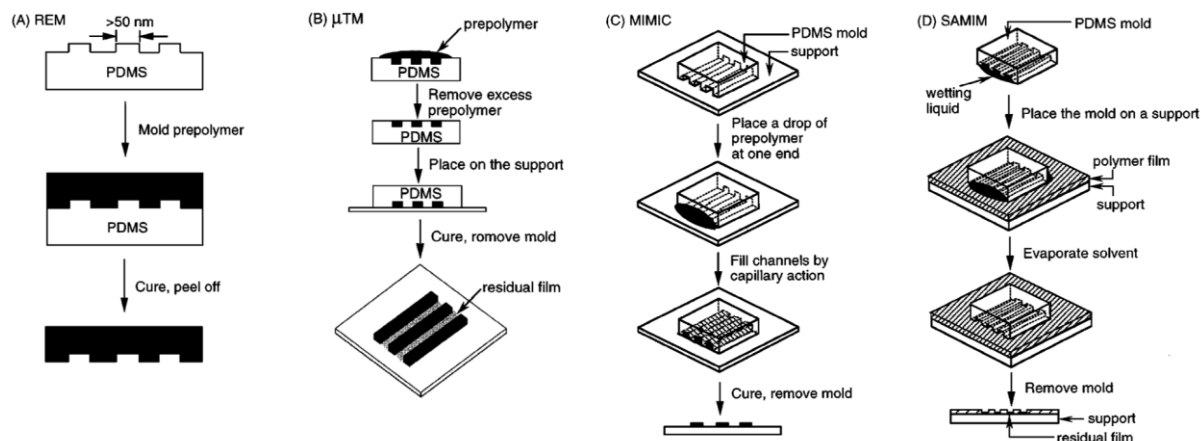
Fig. 1.1. Schematic illustration of procedures for (a) replica molding (REM), (b) microtransfer molding (μTM), (c) micromolding in capillaries (MIMIC), and (d) solvent-assisted micromolding (SAMIM) [6].

For the preparation of micron- and submicron-sized features, various materials have been used, such as ceramics [15, 16], polymers [12, 17], carbon [18] and metals [19, 20]. Microfabrication of ceramics plays an important role in meeting this increasing need [21]. Currently, various 3D

ceramic patterns with different shapes have been prepared, and the size ranges from microns to nanometers [22, 23, 24]. Kim et al fabricated fine-structured ZnO patterns made from mixtures of polyvinyl alcohol and ZnO nano-sized particles via replica molding (Fig. 1.2a) [25]. Hampton et al prepared arrays of sub-500 nm inorganic oxide features using elastomeric perfluoropolyether molds [26]. Veldhuis et al fabricated high-aspect-ratio structures of yttria-stabilized zirconia via micromolding in capillaries (Fig. 1.2b) [15]. These works prove the flexibility of the soft lithography strategy in applying for different materials and shapes.
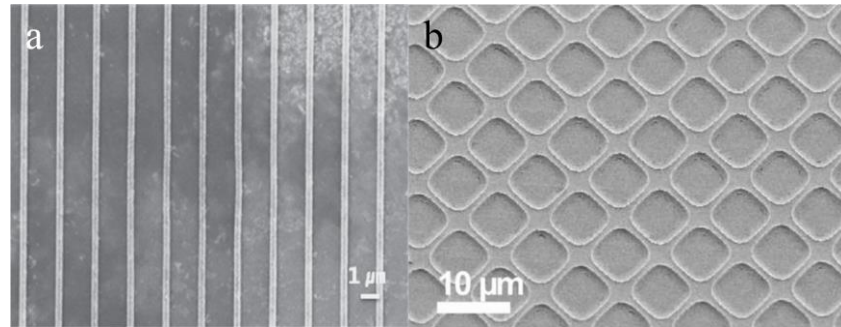
Fig. 1.2. Ceramic patterns prepared via micromolding (a: lines [25]; b: grid [15]).

To create micron- and submicron-sized features using ceramic nanoparticle, suspensions of ceramic nanoparticles are prepared to accelerate the movement of the particles and increase the packing density. To improve the fidelity of the features, there are several requirements about the suspensions. First, in order to reduce the shrinkage during the drying process, a high solid loading (20 % at least) is preferable. Second, since the agglomeration will compromise the quality of ceramic features, well-dispersed suspensions are necessary. Efforts have been put on understanding the dispersion mechanisms properties of various nanoparticle systems, such as the roles of dispersant and the influence of particle size [27, 28]. The effectiveness of utilizing different dispersion mechanisms simultaneously (e.g., electrostatic stabilization and steric stabilization) has been proved [29, 30]. To get ceramic features with good fidelity, the absolute value of zeta potential should be no less than 25 mV [30].

For the micromolding of ceramic features, two aspects should be considered: the patterning process and the drying process. The patterning process involves the filling of suspensions into feature spaces on the molds, and it will determine the fidelity of the ceramic features during the transfering from molds to samples. The drying process will dictate the dimensional changes resulting from the shrinkage. Currently, there are already some techniques that have been developed and utilized to fabricate ceramic features, such as pressure filtration [31], gravitational sedimentation [32], osmotic consolidation [31], and centrifugation [33]. Among these techniques, only centrifugation can benefit the patterning and drying process at

same time. By introducing centrifugal force, the driving force for patterning will be increased and the shear-thinning properties of ceramic nanoparticle suspensions can be utilized. Thus, the patterning process can be accelerated and completed before the suspension loses the flowability due to evaporation of solvent. For drying process, the centrifugal process can increase the packing density of the nanoparticles in suspension, which will reduce the shrinkage during drying process.

1.2 Sintering of ceramic materials

Sintering is the most important step in the processing of ceramic materials. In this process, packed particles are bonded into a coherent object due to the thermodynamic tendency of decreasing its total surface and interface energy [34]. As a major process, sintering has been used to fabricate various ceramic materials with tailored structures and functions, such as doped cerium oxide with high grain boundary density [35], nanocrystalline barium titanate ceramics [36], porous alumina ceramic [37] and dense $(K, Na)NbO_3$-based ceramics with good mechanical and piezoelectric properties [38]. Development of sintering techniques promotes the application of ceramic materials in a broad range of fields, such as fuel cell components [39], electronic packages [40], ceramic-based bioimplants [41], and thermal management [42].

For sintering of dense materials, two key aspects have been focused on achieving full density and limiting the grain size. Because of the competitive relationship between densification and grain growth in consuming interface energy, high relative density and small grain size are hard to obtain simultaneously. Thus, a number of novel sintering techniques, such as high-pressure assisted sintering [43], two-step sintering [44], microwave sintering [45], flash sintering [46], sintering with thermal cycle modification [47], sintering in a reactive atmosphere [48], and spark plasma sintering [49], have been developed to prepare ceramic materials with as-desired structures and properties.

During sintering, particles bond to form a predominantly coherent solid, which involves sample size change and evolution of microstructures [30, 50, 51, 52, 53, 54]. In the past decades, many models and quantitative descriptions have been established and improved to explain the sintering behaviors of ceramic bulks. During sintering, the driving force for atoms transport is the difference in the chemical potential under curved surfaces. In order to describe this process, an ideal model of a powder compact is established to predict the sintering behavior (Fig. 1.3) [55]. Due to the chemical potential difference, atoms are transported from the grain boundary and the particle surface to the neck. When the material transports from the particle surface to the neck, the redistribution of material on the surface of particles will not cause densification.

When the material transport from the grain boundary to the surface of particles, densification and bonding will be induced. Based on the connectivity of the solid and pores, sintering is commonly divided into three stages: initial stage, intermediate stage, and final stage [34]. For the initial stage, the kinetic equations can be expressed as [56]:

$$(\frac{x}{a})^n = F(T)(\frac{1}{a^{n-m}})t \tag{1.1}$$

where a is the radius of the particle, x is the radius of the neck between two particles, $F(T)$ is a function of temperature which includes a diffusion coefficient, and n and m are exponents depending on the transport mechanisms which majorly include surface diffusion, evaporation-condensation, grain boundary diffusion and lattice diffusion. For the intermediate and final stages, the kinetic equations can be expressed as [56]:

$$\frac{1}{\rho}\frac{d\rho}{dt} = \frac{K_1(1-\rho)^k}{G^m\rho} \tag{1.2}$$

where ρ is the relative density, K_1 is a constant, which includes surface energy, temperature, the diffusion coefficient, and molar volume, k and m are exponents depending on the transport path, and G is the grain size. When the pores are attached to the grain boundaries, diffusion-controlled grain growth can be expressed as:

$$\frac{1}{G}\frac{dG}{dt} = \frac{K_2}{G^n(1-p)^l} \tag{1.3}$$

where K_2 is a constant, which contains boundary energy, diffusion coefficient, molar volume, and absolute temperature, and l and n are exponents. The intermediate stage is the major process of the sintering, where materials go through dramatic changes in densification and grain size. Based on the above basic equations, much effort has been devoted to obtaining more precise mathematical expressions for specific systems. Based on the ideal model of a powder compact on sintering, Maximenko et al analyzed the neck growth rate between rigid spherical particles during sintering and estimated the value of diffusion coefficient in solid-state sintering [57]. Kang et al examined the classic geometrical model of final stage sintering (bcc-packed tetrakaidecahedral grains with spherical pores at 24 corners of a grain) and presented a new diffusion model and kinetic equations which explained the role of grain boundaries and the diffusion area in the densification process [58]. Bernard-Granger et al studied the relationship between grain size and relative density and utilized it to analyze the sintering mechanism [59]. Aiming at the coarsening in sintering, German studied the distributions of grain size and grain shape, and grain growth kinetics [60]. These efforts improve the understanding of the sintering behaviors, especially about densification and grain growth.
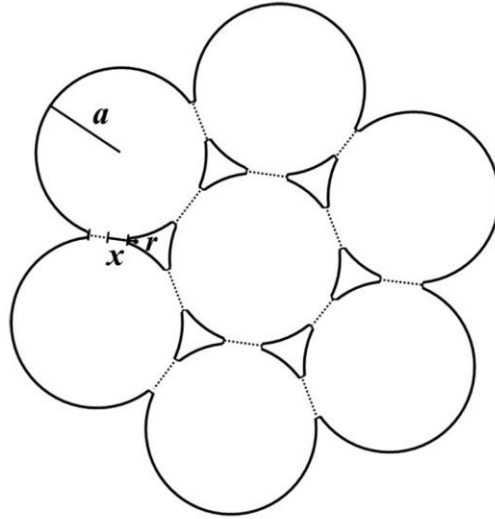
Fig. 1.3. An ideal model of a powder compact on sintering. (a: The radius of the particle; x: the radius of the neck between two particles; r: the radius of curvature of the neck)

In a sintering process, sintering mechanisms dictate sintering behaviors such as grain growth, densification, and pore elimination [61, 62]. For solid-state sintering, the sintering process of particles is driven by the chemical potential difference resulting from the curved surface [34]. For conventional ceramics, four main sintering mechanisms occurring at the atomic level are grain boundary diffusion, volume diffusion, surface diffusion, and evaporation-condensation [63, 64, 65]. Among them, diffusion via grain surface (surface diffusion) and evaporation-condensation influence grain coarsening, while grain boundary diffusion and volume diffusion (trapped pore removal) are principally responsible for densification [63, 66, 67, 68]. For a sintering process, all the sintering mechanisms work simultaneously. Different contributions of the mechanisms result in the various sintering behaviors. Therefore, understanding the contribution and roles of these different sintering mechanisms is a critical step in controlling the sintering behaviors of ceramic materials [61, 69, 70, 71].

1.3   Sintering of micron-sized ceramic features

With the miniaturization of various components and devices, understanding the sintering mechanisms and the related kinetics of small features (down to micron-size at least) becomes very important. When the sample size is down to micron size, researchers found some new sintering phenomena that were quite different from the bulk materials. For example, Martin et al patterned $Pb(Zr_{0.52}Ti_{0.48})O_3$ thin films by micromolding in capillaries, and found "double-peak" film topographies resulting from the nonuniform densification of the gel matrix [72]. Veldhuis et al fabricated high-aspect-ratio micron- and submicron-sized yttria-stabilized zirconia patterns using micromolding in capillary and found that the sintering process resulted

in crystallization of the amorphous structures and more shrinkage [25]. Rosqvist et al fabricated lead zirconate titanate thick films with lateral by replica micromolding and following sintering, and discussed the stochastical bending phenomenon of the features [73]. Based on these works, it can be known that ceramic features show some special sintering behaviors that are not found in the sintering process of ceramic bulks. It demonstrates that sintering process has a quite different influence on the morphology, microstructure and properties of the ceramic features compared to the ceramic bulks. However, current research still stays on the discussion about the specific sintering behaviors, and the fundamental theory should be studied and established.

When the feature size is down to the micron scale, contributions of the sintering mechanisms may differ markedly from those of larger size components because of the difference in the ratio of vapor/solid surface to solid/solid interface [74, 75, 76, 77, 78, 79]. As a result, small size features may exhibit different microstructural evolution and densification rate in comparison to bulk samples. For example, an increase in vapor/solid surface will enhance the effect of surface diffusion and slow down the densification rate. So far, little attention has been paid to the densification and microstructural evolution of micron-sized features from sintering mechanism point of view. However, such understanding is necessary for predicting the sintering behaviors and outcomes of micron-sized ceramic features, which will benefit the fabrication of small-sized components with desirable properties.

When grain size is comparable or larger than pattern size, because of the lack of grain boundaries, the major driving force of sintering is the curvature gradient of grain surfaces. Thus, the surface diffusion and evaporation-condensation mechanism will play more important roles in the sintering process of ceramic features in comparison to that of ceramic bulks. For surface diffusion, diffusion matter flux along free surfaces of particles J_s can be expressed as [57]:

$$J_s = -\frac{\delta_s D_s \Omega \gamma_s}{kT}\frac{dK}{ds} \tag{1.4}$$

where δ_s is the thickness of the surface layer in which the diffusion takes place, Ω is the atomic volume, γ_s is the specific surface energy, k is the Boltzmann's constant, K is the sum of the principal curvatures at the edge of the neck, s is the curvilinear coordinate along the particle surfaces, and T is the absolute temperature. For evaporation-condensation, the mechanism is affected directly by vapor pressure, which can be affected by activation energy, temperature and surface curvature. According to the Langmuir adsorption equation, the flux of deposited material can be expressed as [80]:

$$J_d = \alpha(P_1 - P_0)(\frac{1}{2\pi RTM})^{1/2} \tag{1.5}$$

where α is the accommodation coefficient, P_1 is the vapor pressure over a small negative radius of curvature, P_0 is a pre-exponential constant, V_m is molar volume, M is the molar weight, and R the gas constant. Since the fundamental sintering mechanisms are applicable for both bulks and features, the above models still can be used to estimate the atomic fluxes via the two sintering mechanisms and furtherly analyze the sintering behaviors of ceramic features.

ZnO has been widely used in electronics, photonics, acoustics, and sensing due to its unique characteristics, including high excitation binding energy, wide bandgap, and desired piezoelectric response [81, 82]. The sintering behaviors of bulk ZnO are well-known and understood [83, 84, 85, 86]. However, the study of micron-sized ZnO components is scarce. Kim et. al investigated the shrinkage process of micron-sized ZnO patterns and found that the patterns were destroyed during the late stage sintering [25]. Ye et. al. studied the sintering behaviors of submicron-sized ZnO features with ~50 vol% polyvinyl alcohol binder [87]. Although we have gotten some information about the sintering behaviors of ceramic features, there are still some problems. First, the high binder content compromised the applicability of the related conclusions. Second, current progress still stays on the preliminary observation and theoretical analysis based on ceramic-polymer systems. Therefore, sintering study of pure micron-sized ZnO features has great application significance, for the ZnO material itself and the sintering process in general.

1.4   Objective

The ultimate objective of this work is to fabricate micron- and submicron-sized ceramic patterns with high fidelity and understanding the related micromolding and sintering mechanisms. For the micromolding process, the introduction of an extra centrifugal force has an influence on the driving force and patterning rate. The relationship between centrifugal force and pattern fidelity should be understood quantitatively and the conditions for getting ceramic patterns with high fidelity should be suggested. For the sintering process, the sintering behaviors of micron- and submicron-sized ZnO features are studied. The effects of geometry factors and sintering conditions are discussed. Feature evolution and surface roughening are explored and characterized. The difference in sintering behaviors between features and bulks is studied. Besides, different atmospheres are used to sinter micron-sized ZnO ridges. The effect of atmospheres on sintering is studied by analyzing the differences in the morphological and microstructural evolution. Fundamental theories and mathematic expression are established to explain the evolution of microstructures.

2 Centrifuge-aided Micromolding of Micron- and Submicron-sized Patterns

2.1 Introduction

Device miniaturization requires effective approaches to fabricate components with small sizes. Microfabrication of ceramics has gained considerable attention due to its great potential to meet this increasing need [21]. At the same time, soft lithography has attracted great interest in the fabrication of micro- and nano-structures since the 1990s [6]. Using soft lithography, high-quality 3D patterns can be obtained on both planar and curved surfaces, and the size range is from microns to nanometers [22, 23, 24]. To date, many kinds of soft lithography techniques have been developed, such as replica molding [7, 8], microtransfer molding [11, 88], micromolding in capillary [12], solvent-assisted micromolding [14], nanotransfer printing [4], decal transfer lithography [9], and nanoskiving [13]. Various materials have been used to prepare micro-features, such as polymers [17, 89], macromolecules [90], metals [20, 91], carbon [18], and ceramics [15, 92].

When ceramic nanoparticles are used as the starting materials for microfabrication, the low flowability and extremely loose packing of particles limit the patterning ability. Proper suspensions with high particle mobility should be created in order to accelerate the particle movement into the features and pack densely. To produce micron and submicron-sized features from ceramic nanoparticle suspensions, two aspects should be closely examined: the filling process and the drying process. The filling process determines the replication capability of features from the patterning molds, and the drying process dictates the dimensional changes from the shaped wet particle packing to dry feature arrays.

For the filling process, the colloidal suspension, as the carrier of particles, plays a critical role. Suspension flow behaviors directly affect the fidelity, surface roughness, and microstructures of the obtained features [93]. Efforts have been devoted to understanding the dispersion mechanisms and dispersibility of various nanoparticle systems, such as the roles of dispersant and particle size [27, 28]. To improve the quality of a colloidal suspension, strategies that utilize different dispersion mechanisms (e.g., electrostatic stabilization and steric stabilization) simultaneously have been proved effective [29, 30]. Related to the patterning driving force, several techniques have been developed to control the flow behavior, such as gravitational sedimentation [32], osmotic consolidation [31], pressure filtration [31], and centrifugation [33]. In addition, features can be categorized as convex and concave. For convex features, the filling process can proceed from both the top and the side along with easier trapped air removal; fluid movement is the dominant factor in influencing the filling of the patterns.

For concave features, diffusion is the major process in removing trapped air because of the restriction of the feature architectures.

For the drying process, in order to decrease the feature shrinkage, a suspension with high solids loading is preferred. However, the suspension with a high solid loading loses fluidity quickly as a result of solvent evaporation; the filling process should be finished in a short time. This can be accomplished either by increasing the patterning driving force or by improving the flowability of the suspensions. For shear-thinning suspensions, these two aspects can be achieved simultaneously. In addition, during the accelerated patterning process, particles can pack more densely, which may decrease the feature shrinkage during drying.

In our previous work, ZnO rods of 250-750 nm size with an aspect ratio of ~ 1:1 were made by direct casting [94]. However, because the diffusion of trapped air is slow, for larger size patterns (> 1 μm^3), the diffusion process of trapped air into the suspension cannot complete before the suspension loses desired flowability due to evaporation of the solvent. Moreover, because of the increased surface area of the features during the filling process, large surface tension resists the filling process. Thus, extra driving forces need to be introduced to accelerate this process.

In this study, centrifuge-aided micromolding was used to prepare micron- and submicron-sized ZnO features. The flow behavior of the ZnO suspension and the fidelity of the as-prepared features were characterized. The effects of the centrifugal force on the feature cavity filling process by the suspension and on the patterned feature shrinkage during the drying process were studied. The influence of the centrifugal force on the diffusion of trapped air was analyzed. The applicability of this method was also tested using a ZrO_2 nanoparticle suspension.

2.2 Experimental procedures

2.2.1 Focus ion beam (FIB) patterning

Micron- and submicron-sized feature patterns were made on a silicon wafer by focused ion beam (FIB) lithography (Helios NanoLab 600 Dual Beam, FEI Company, Hillsboro, OR). The FIB voltage was 30 kV and the beam current was 2.8 pA. Ridges with sizes from 2 μm to 500 nm and rods with a size of 2 μm were patterned into arrays. Both kinds of features had an aspect ratio of ~ 1:1. The heights of the features were controlled by the patterning time and can be easily varied.

2.2.2 Preparation of poly(dimethylsiloxane) molds

Sylgard silicone elastomer 184 (poly(dimethylsiloxane) (PDMS)) and the accompanying curing agent (Dow Corning Corporation, Greensboro, NC) with a weight ratio of 10:1 were mixed. After adding 3 wt% Triton X-100 (TX-100, $C_{14}H_{22}O(C_2H_4O)_n$; Sigma-Aldrich, St. Louis, MO) (based on the total weight of the silicone elastomer and the curing agent), the mixture was vacuumed in a chamber for 1 hr to deair the pre-polymer. Then the mixture was poured onto the patterned silicon wafer. The assembly was placed in vacuum until no bubbles were observed before being cured at 120°C for 2 hrs. After cooling to room temperature, the PDMS mold was carefully peeled off from the silicon wafer.

2.2.3 Centrifuge-aided micromolding

For the ZnO aqueous suspension used for the micromolding, ZnO nanoparticles (Nanostructured and Amorphous Materials, Inc., Houston, TX) with an average particle size of ~25 nm were used as the starting material. A poly(acrylic acid) (PAA) solution (Mw 1800; Aldrich, St. Louis, MO) was used as the dispersant and binder simultaneously. The suspension was prepared by batch addition of ZnO and 4.5 wt% PAA solution (based on the weight of the ZnO powder) into a diluted ammonia solution with a pH value of 11. Then, the mixture was dispersed by a vibratory mill (SPEX 8000 Mixer Mill; SPEX SamplePrep LLC, Metuchen, NJ) for 15 mins. This process was repeated three times to obtain a well-dispersed suspension with a solid loading of ~30 vol%.

Centrifuge-aided micromolding was illustrated in Fig. 2.1. First, the as-prepared suspension was added into the PDMS mold. Then, the suspension-filled mold was fixed with an epoxy holder in a centrifuge tube. The centrifugal speeds were set from 0 to 10,000 rpm, respectively. After the centrifuge-aided micromolding, the mold with a deposited ZnO layer was taken out and the solvent layer on the top was removed. The drying process proceeded in air at room temperature for about 48 hrs. Finally, the dried ZnO sample with micron- to submicron-sized feature patterns was taken out from the PDMS mold.
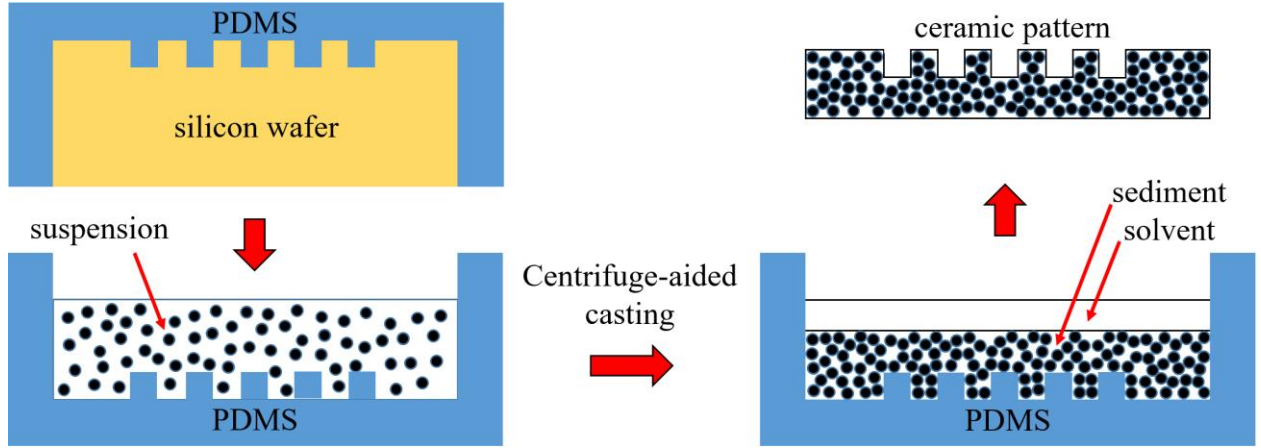
Fig. 2.1. Schematic of centrifuge-aided micromolding.

2.2.4   Characterization

Viscosity measurements of the suspensions were conducted using a rheometer with a cone-plate geometry (AR 2000; TA Instruments, New Castle, DE). The density of the suspensions is calculated based on the content. The relative density of the dry ZnO samples was measured by the Archimedes' method. Feature fidelity was evaluated using scanning electron microscopy (SEM, Quanta 600 FEG; FEI Company, Hillsboro, OR) to determine the line-edge roughness (LER) and inverse circularity (IC) of the features [95]. In order to focus on the quality of the ridges, the broken parts of the ridges were avoided. To obtain LER for ridge features, software ImageJ with the plugin Analyze Stripes was used to determine the average feature size of the ridges and the corresponding standard deviation. First, a SEM image was cropped so that only the features were visible. Then the image was converted to greyscale and the contrast was heavily increased. The software established the position of each line based on the greyscale values and measured the distance in pixels between two lines. From the data, the ridge width and standard deviation of that measurement were isolated. The LER values represented the line-edge roughness as a percentage of the feature size.

Inverse circularity (IC) represented the derivation of feature circularity from an ideal round shape, which was used as a gauge for the patterned rod dimensional fidelity. IC was calculated as follows.

$$IC = 4\pi \times \frac{Area}{Perimeter^2} \tag{1.1}$$

IC value was similarly obtained using the Analyze Particles plugin in ImageJ.

2.3 Results and discussion

2.3.1 ZnO suspension flowability

In our previous work, 3 wt% PAA was used to obtain well-dispersed suspensions [94, 96, 97, 98, 99]. However, 4.5 wt% PAA was added in this study in order to resist the damage from the relative movement between the mold and the sample during the demolding process [100]. Even with the increased PAA amount, Fig. 2.2 shows the viscosities of the as-prepared ZnO suspension decrease exponentially with the shear rate increase, a typical shear-thinning behavior. When the shear stress increases from 41.4 to 153.9 Pa, the viscosity decreases from 7.7 to 0.27 Pa·s, a 96.5% drop, demonstrating the non-Newtonian fluid characteristic of a decreasing viscosity trend with the shear rate. As a comparison, the zero shear rate viscosity for water and acetone are 0.894 mPa·s [101] and 0.306 mPa·s [102], respectively. Thus, the ZnO suspension is much more viscous than common liquids. On the other hand, an alumina suspension (30 vol% solid loading, 2 wt% PAA dispersant, pH 11) used for suspension casting has 3 Pa·s viscosity [96], accordingly, the ZnO suspension is fluid enough under shear for molding. Specifically, for current system, the viscosity is controlled at no more than ~ 5 Pa·s. During the feature cavity filling process at 0-10,000 rpm centrifugal speed, the shear stress-viscosity curve along the feature cavity surface can be calculated as shown in Fig. 2.6 based on the well-known Williamson model [103]. The results indicate that the ZnO suspension should have low viscosities and thus high fluidity during the centrifuge-aided patterning process to quickly complete the feature cavity filling. After the suspension fills the feature cavities, the ZnO nanoparticle movement is driven by the pressure difference between the top and bottom of the features. The centrifugal force determines the pressure difference. Besides, based on our previous work, in order to obtain good dispersibility, ammonia is used to keep the pH value of suspension at 11 so that the absolute value of zeta potential is >25 mV [94]. Meanwhile, since ammonia will evaporate with the water during the drying process, no residue will be left in the dry samples.
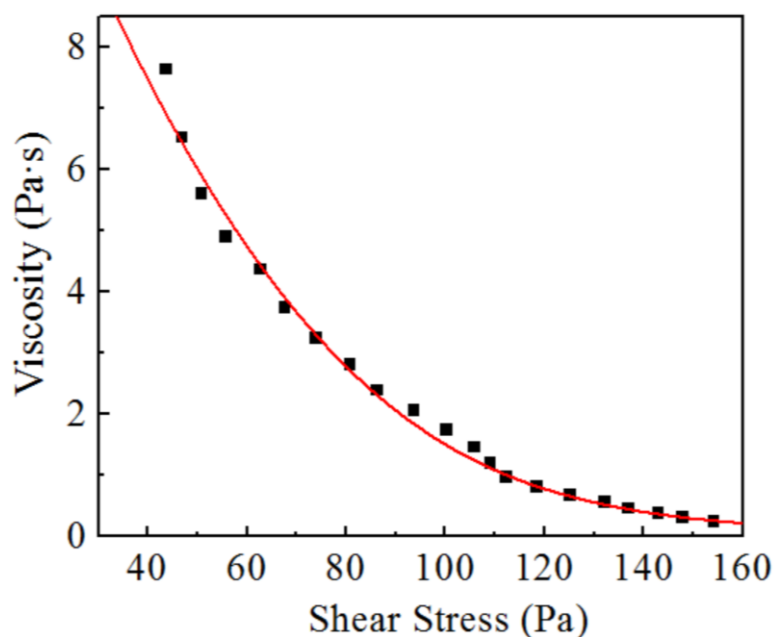
Fig. 2.2. Viscosities of ZnO nanoparticle suspensions with 30 vol% solid loading and 4.5 wt% PAA (The solid line is the fitting result using the Williamson model [103]).

2.3.2 Micron- and submicron-sized ridge and rod patterning

Fig. 2.3 shows the SEM images of the ZnO ridges prepared under a centrifugal speed of 7000 rpm. Based on Fig. 2.2, for the ridges with the size of 1.9, 0.8 and 0.4 µm, the shear stress is 121.4, 51.1 and 25.6 Pa respectively, which means that a corresponding suspension viscosity of ~0.75, 5.8 and 10 Pa·s is involved in the cavity filling process. The sizes of the ridge features in Fig. 2.3a, 2.3b, and 2.3c are ~1.9, 0.8, and 0.4 µm respectively. For the ridges larger than 0.8 µm (Figs. 2.3a and 2.3b), intact features are obtained with no distortion. When the size of the ridges is 400 nm (Fig. 2.3c), defects can be found on parts of the ridges. This results from the relative movement between the pattern and the mold as to be explained next.
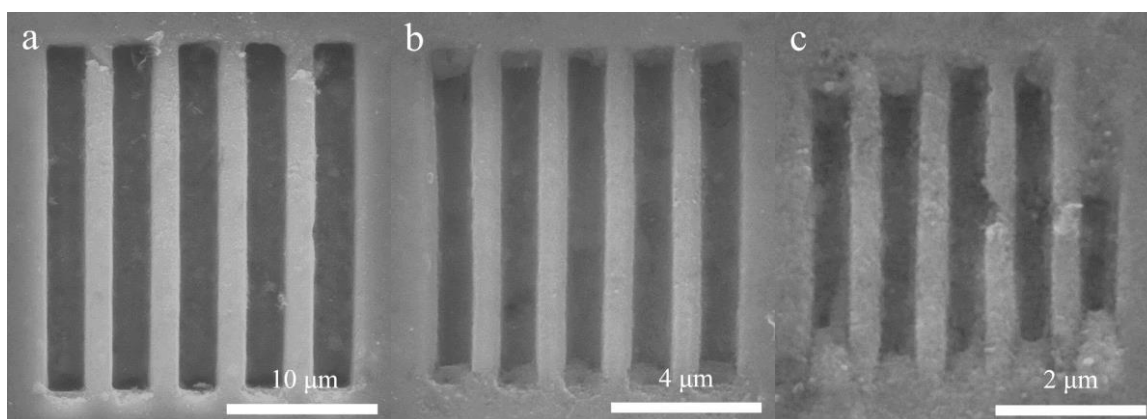
Fig. 2.3. SEM top images of ZnO ridges prepared under 7,000 rpm centrifuge condition (a: 1.9 µm ridges, b: 0.8 µm ridges, c: 0.4 µm ridges).

Fig. 2.4 shows the SEM image of the 2 μm ridge pattern prepared without any centrifugal force. Only incomplete features can be obtained. Based on the long holding time of the suspension in the PDMS mold (about two weeks), we conjuncture that the incomplete features are a result of incomplete micromolding and poor particle packing in the feature cavity. After drying, loose particle packing collapses and only part of the features are formed. With the aid of the centrifugal force, the increased driving force for the suspension filling of the feature cavities under the decreased viscosity of the suspension and the accelerated particle packing both contribute to the high fidelity of the ZnO ridges.
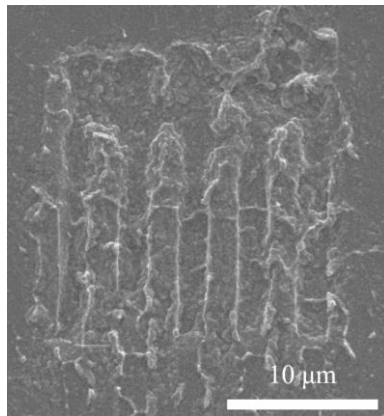
Fig. 2.4. SEM image of the 2 μm ZnO ridge patterns prepared without any centrifugal force (top view).

Fig. 2.5 shows the LER measurements of the ZnO ridges with different sizes. All the LER values are less than 5% and decrease with the feature size increase, consistent with the SEM images in Fig. 2.3. When the ridge size decreases from 1.9 to 0.4 μm, the LER value increases from 1.9% to 4.3%; the corresponding standard deviation also increases with the ridge size from 0.57% to 1.37%. However, the LER value is a relative number based on the size of the ridge. The absolute roughness values of the ridges with different sizes are very close due to the same suspension and micromolding process used. When the ridge size is down to ~400 nm, the effect of large particles (~40 nm) on feature fidelity loss can be observed clearly.
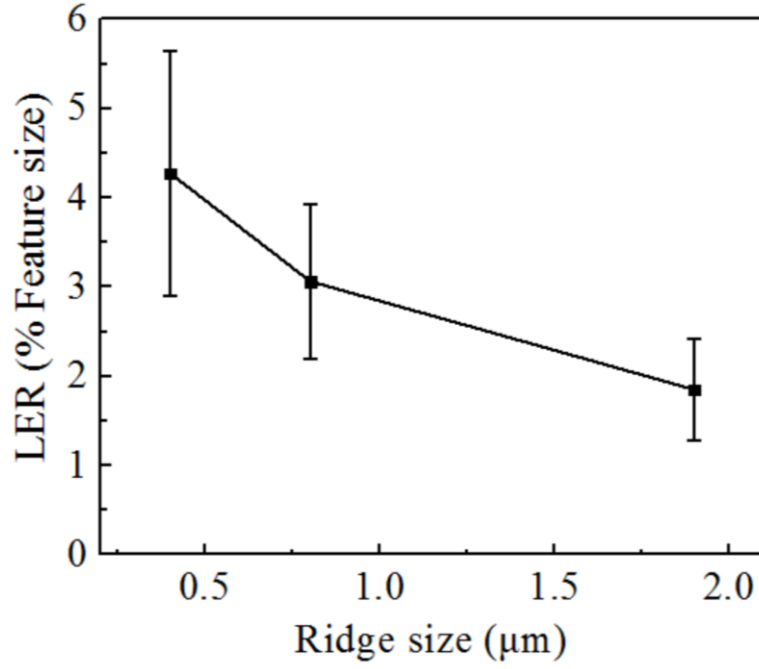
Fig. 2.5. LER values of ZnO ridge arrays with different feature sizes.

Fig. 2.5 shows that the LER value is still less than 5% when the ridge size is down to 400 nm. In order for the patterns derived from the centrifuge-aided molding to be useful in a given device application, maximum values for LER needs to be established. Literature suggests that the LER limit is set at ≤10% of the feature sizes [104, 105, 106], which indicates that the features fabricated in this study are acceptable.

The fundamental patterning process for the ridge features can be understood as follows. Because of the convex architecture of the ridge features on the mold, a fluid pressure difference is produced between the top and the bottom of the ridge cavities during patterning. The pressure pushes the liquid interface into the cavities and the trapped gas escapes out simultaneously. The linear flow rates can be estimated by [107]:

$$\frac{dl}{dt} = \frac{a^2 P_i}{24\eta l} \tag{1.2}$$

where l is the distance of the interface movement in time t, a is the ridge size, P_i is the pressure on the interface, η is the viscosity of the suspension. For the ridges, the filling rate should be affected by the pressure difference and the viscosity of the suspension. When the feature space is occupied by gas, the average pressure difference on the interfaces can be estimated by:

$$P_i = \rho G \frac{a}{2} \tag{1.3}$$

where ρ is the density of the suspension (2.3 g/cm^3) and G is the equivalent gravity acceleration in the centrifugal environment. On the other hand, because the ZnO suspension is shear-

thinning, the viscosity decreases exponentially with increased shear stress. According to the Williamson model [103], the viscosity η can be estimated by:

$$\eta = \frac{\eta_0}{1+(k\gamma)^n} \tag{1.4}$$

where η_0 is the zero-rate viscosity (16.41 Pa·s), k is s the consistence index (0.23), γ is the shear rate, n is the flow behavior index (0.84), the values of k and n are obtained by fitting the plot in fig. 2.2. In the current system, the shear stress can be estimated as the fluid pressure. Based on equations (1.3) and (1.4), the filling time is:

$$t = \frac{24\eta l^2}{a^2 P_i} = \frac{42.8\eta l^2}{a^3 \rho r K^2} \times 10^5 \tag{1.5}$$

where r is the centrifugal radius, K is the centrifugal speed. Thus, the pattern filling time is proportional to the viscosity of the suspension and inversely proportional to the square of the centrifugal speed. The relationships of viscosity and pressure on the interface vs centrifugal speed for different ridge sizes are shown in Fig. 2.6. Both the feature size to be patterned and the centrifugal speed play significant roles in the suspension follow and cavity filling.
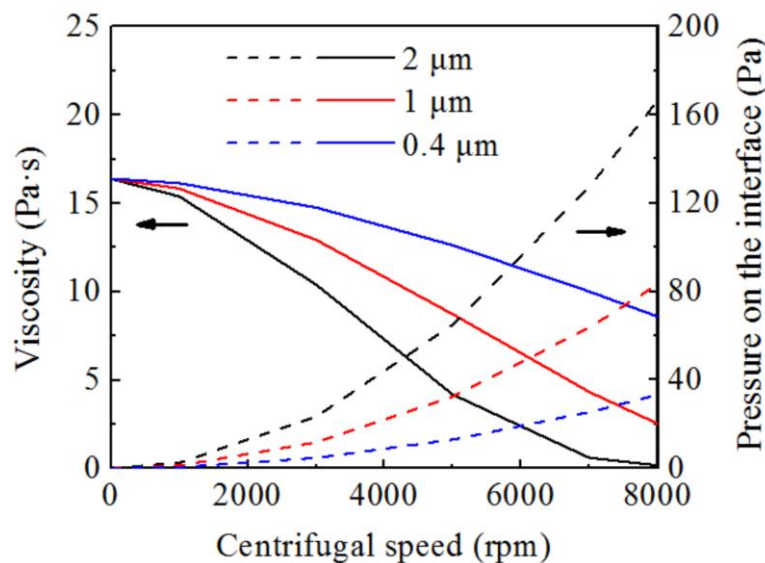
Fig. 2.6. Effects of the centrifugal speed on pressure on the interface (dash line) and viscosity (solid line) for ridges with different size.

Considering the ridges with different sizes, when the ratio between the width, height, and length are 1:1:10, the relationship between the feature cavity filling time and the ridge size is shown in Fig. 2.7. Ridges with smaller sizes need longer filling time due to the decreased pressure on the interface. As predicted, ridges with larger sizes need shorter filling time, and higher centrifugal speed can reduce the filling time. As a specific example, when the centrifugal speed is 7000 rpm, for 1 μm ridges, the pressure on the interface will increase from 0.01 Pa to 64 Pa and the viscosity will decrease from 16 to 4 Pa·s compared to the micromolding in a

natural gravitational environment. In order to fill a 1 μm ridge space, the filling time decreases from 1,067 hrs to 2.5 mins. This also means that it is impractical to let the suspension fill into the micro-cavity under a gravitational environment. However, it is fairly easy to be achieved under a centrifugal molding condition.
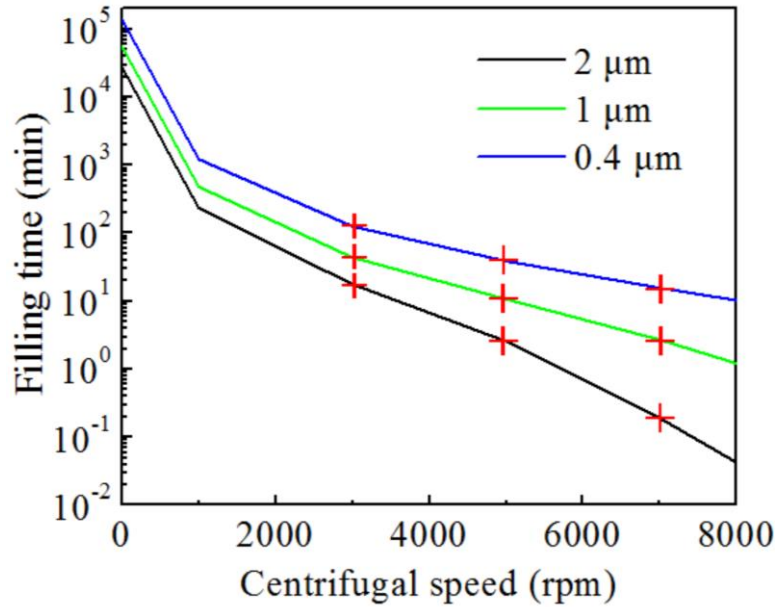
Fig. 2.7. Effects of the centrifugal speed on the filling time for ridges with different sizes (The points with cross marks are the calculated values based on the conditions used in the experiments).

During the centrifuge-aided molding process, the deposited particles pack and form an interconnecting network. Different from the direct casting process without any centrifugal aid, an intermediate state is introduced between the suspension state and the dry state during the centrifuge-aided micromolding process, which can be called sediment state. With the increase of the centrifugal force, the applied pressure on the nanoparticle network increases correspondingly. As explained, the sediment state has a varying degree of particle packing depending on the centrifugal force. When the pressure exceeds a critical value, the particles in the network rearrange and the particle packing will irreversibly collapse to form a denser network [31]. The mean centrifugal pressure P_M is a power-law function of the average packing volume fraction $\varnothing_a$ of the particle sediment layer, which can be expressed as [108]:

$$P_M = \beta \varnothing_a^n \tag{1.6}$$

where β and n are the coefficients that depend on the properties of the particles and the suspensions. In our work, the packing behavior of the ZnO suspension agrees with the power-law function of equation (6). The parameters of β and n can be fitted to be 1.1×10^9 (MPa) and 21, respectively. Higher centrifugal pressure will result in higher sediment packing fraction.

17

For the ZnO suspension at 7,000 rpm centrifugal speed (0.31 MPa pressure), the average packing volume fraction is 34.4 vol%, while at 3,000 rpm centrifugal speed (0.06 MPa pressure), the average packing volume fraction is 33.4 vol%.

During the centrifuge casting, the suspension applies an increased pressure on the surface of the mold with the increase of the centrifugal speed. Higher centrifugal pressure also causes more elastic deformation of the PDMS mold. The ultimate compressive strength for PDMS is 28.4–51.7 GPa [109], which is strong enough to bear the compression from the ceramic suspension. Based on the understanding of fluid statics, the elastic deformation of the PDMS mold can be estimated by:

$$\sigma = \rho G h \qquad (1.7)$$

$$D = \frac{\sigma}{E} v \qquad (1.8)$$

where σ is the fluid static pressure on the mold, ρ is the density of the suspension (2.38 g/cm^3), G is the equivalent gravity acceleration, h is the thickness of the suspension layer (5 mm), D is the amount of elastic deformation in the horizontal direction, E is the compressive modulus, and v is the Poisson ratio. For the current system, the PDMS mold is cured at 120 ^{o}C and has a compressive modulus of ~140 MPa with a Poisson ratio of 0.5 [110]. The PDMS elastic deformation at different centrifugal speeds is shown in Fig. 2.8. When the centrifugal speed reaches 10,000 rpm, the amount of the elastic deformation of the PDMS mold in the horizontal direction is ~0.47%. Considering the LER values of the ridges (1.9%-4.3%), the deformation can reach 25% of the LER value at most. So, the influence of the deformation on the LER values cannot be neglected. For the ridges with smaller sizes, this phenomenon will become more obvious due to the higher LER values. Thus, there is a high possibility that the fidelity of the ridges will be deteriorated at the centrifugal speed of 10,000 rpm. When the centrifugal speed decreases to 7,000 rpm, the deformation decreases to ~0.23%. The chance of feature damage is much lower. To minimize such elastic deformation, the highest centrifugal speed should be limited to 7,000 rpm in order to keep the deformation less than 0.25%.
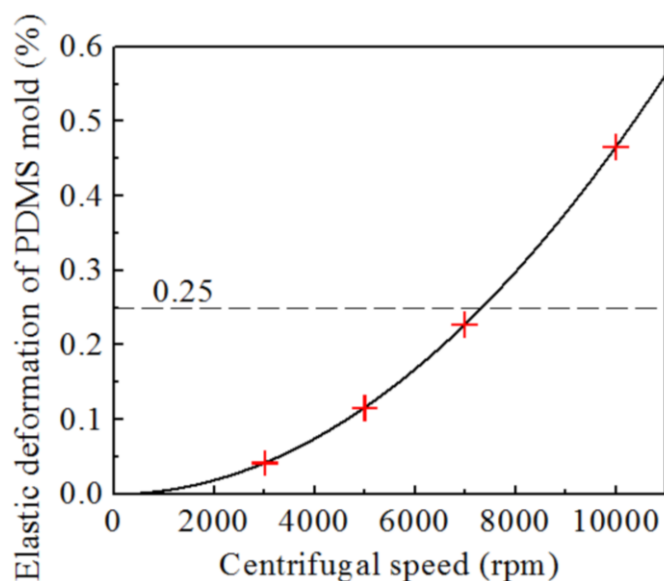
Fig. 2.8. Elastic deformation of the PDMS mold in the horizontal direction at different centrifugal speed (The points with cross marks are the calculated values based on the conditions used in the experiments).

Another aspect to consider is the strength of the cast samples. The cast wet samples have much lower strength than the dried samples. Even the dried green samples only have a strength less than 0.2-1.6 MPa [111, 112]. For the wet samples, the strength would be even lower and damages can occur easily. The smaller size ridges cannot tolerate the stress because of their small sizes (and thus high stress) and are more likely to be damaged.

Fig. 2.9 shows the SEM images of the rod patterns prepared with and without the centrifugal force. The average diameter is 1.58±0.10 μm. With the centrifugal force, all the features show well-defined round shapes. The average IC value is 0.92±0.02, which is close to that of the perfect rod, 1.0. In contrast, without the aid of the centrifugal force, only shallow plateaus can be found (Fig. 2.9b). The centrifugal force consistently facilitates the patterning process.
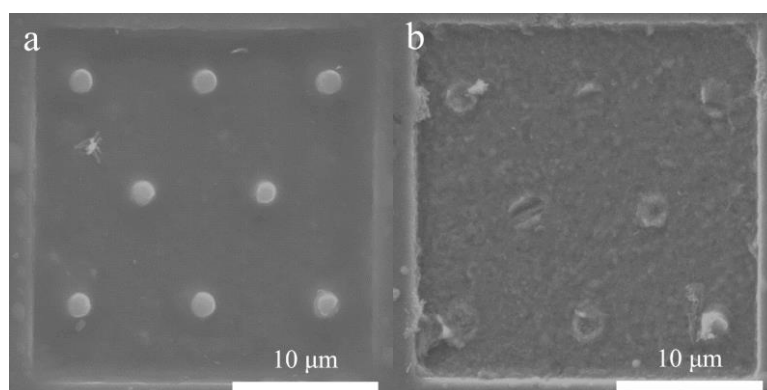
Fig. 2.9. SEM images of ZnO rods with an average diameter of 1.58 μm prepared with (a: top view) and without the centrifugal aid (b: top view).

2.3.3 Trapped air diffusion during patterning

As stated earlier, rods with a diameter from 200 to 750 nm were prepared using direct casting without any centrifugal force [94]. However, the key problem is the removal of trapped air in the designed feature space. Micron-sized features need a long diffusion time (at least a few hours) to remove trapped air. Depending on the patterned feature size, the filling process can be controlled by the instability of the suspension-trapped air interface [113]. The critical diameter can be estimated using the following equation [114]:

$$D_c = \pi\sqrt{\gamma/G(\rho_s - \rho_g)} \tag{1.9}$$

where γ is the surface tension of the suspension (59 mN/m) [94], ρ_s is the density of the suspension and ρ_g is the density of trapped air. For a specific suspension, the critical diameter depends on the centrifugal speed and the relationship is shown in Fig. 2.10. In the current system, the interface stability is determined by the feature size and the equivalent gravity. The critical diameters at 3,000, 5,000 and 7,000 rpm should be 157, 94 and 67 μm. So, the stability of the suspension-trapped air interface is not of concern and will not be considered further.
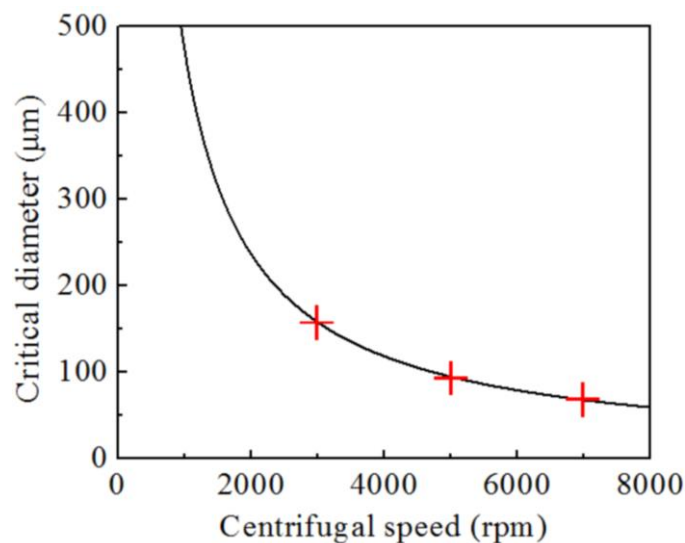
Fig. 2.10. Critical diameters at different centrifugal speeds (The points with cross marks are the calculated values based on the conditions used in the experiments).

Trapped air removal depends on the diffusion process through the suspension. In this study, the introduction of the centrifugal force accelerates the diffusion by increasing the pressure at the suspension-trapped air interface. The diffusion rate is determined by the concentration gradient of dissolved air across the suspension from the trapped air location to the atmosphere. Since the atmosphere pressure is constant, the pressure of trapped air determines the diffusion rate, which can be estimated based on the Young-Laplace equation:

$$P = \frac{2\gamma}{R} = \frac{4\gamma\cos\theta}{d} + \rho Gh + P_0 \tag{1.10}$$

where θ is the contact angle (76°), d is the diameter of the rods, and P_0 is the atmosphere pressure. The relationship between the pressure and the centrifugal speed is shown in Fig. 2.11. According to Henry's law:

$$C=k_{H, CP} \times P \qquad (1.11)$$

where C is the concentration of dissolved air, $k_{H, CP}$ is the Henry's law constant of air in water (1.0×10^{-3} mol/L/atm), and P is the pressure. When the centrifugal force is 7,000 rpm, the pressure increases from 130 kPa to 769 kPa. The concentration of air at the interface will increase from 1.30×10^{-3} mol/L to 7.69×10^{-3} mol/L. So, the concentration difference across the suspension increases from 0.29×10^{-3} to 6.68×10^{-3} mol/L. Since the diffusion rate is controlled by the concentration gradient of dissolved air near the interface, which is proportional to the concentration difference across the suspension [94], the diffusion rate will be accelerated by the centrifugal force.

The relationship between the centrifugal speed and the diffusion time is shown in Fig. 2.11. When the centrifugal speed is at 7,000 rpm the diffusion rate will increase by ~23 times. Thus, for a rod with the diameter of 2 μm, only 13 minutes are needed to complete the filling process. Without the centrifugal aid, the process could be prolonged to 5 hrs, the diffusion process will not be over until the evaporation of water becomes dominating, which leads to an air bubble locked-in system after drying.
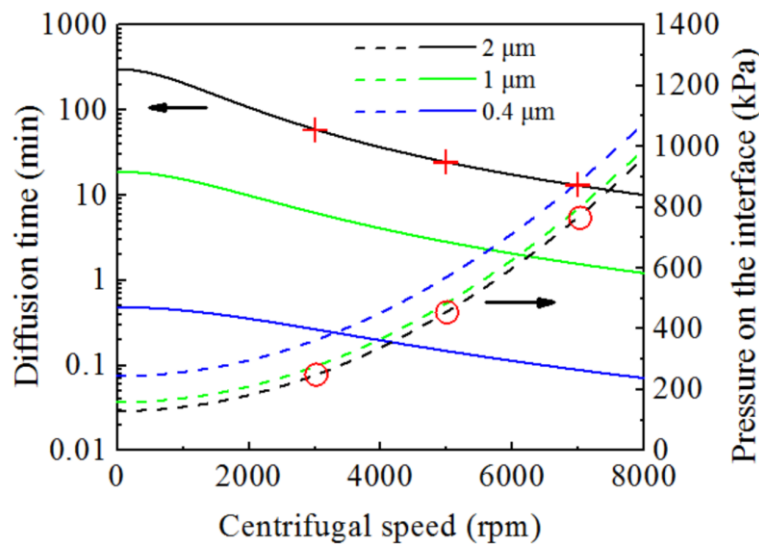
Fig. 2.11. Relationships between the pressure on the interface and the centrifugal speed (black) and between the diffusion time and centrifugal speed (blue) for the ZnO rods with different sizes (The points with cross marks are the calculated values based on the conditions used in the experiments).

2.3.4 Patterned array drying

Fig. 2.12 shows the relative densities of the dried samples prepared under the centrifugal speed from 0 to 10,000 rpm, which range from 39.9% to 42.9%. When no centrifugal aid is used (the centrifugal speed at 0 rpm), some micron-sized air bubbles are trapped in the suspension because of the high viscosity of the suspension, and then in the dry samples, which slightly lowers the relative density. For the dry samples prepared with the centrifugal aid, similar relative densities are obtained for different centrifugal speeds, at ~41%.
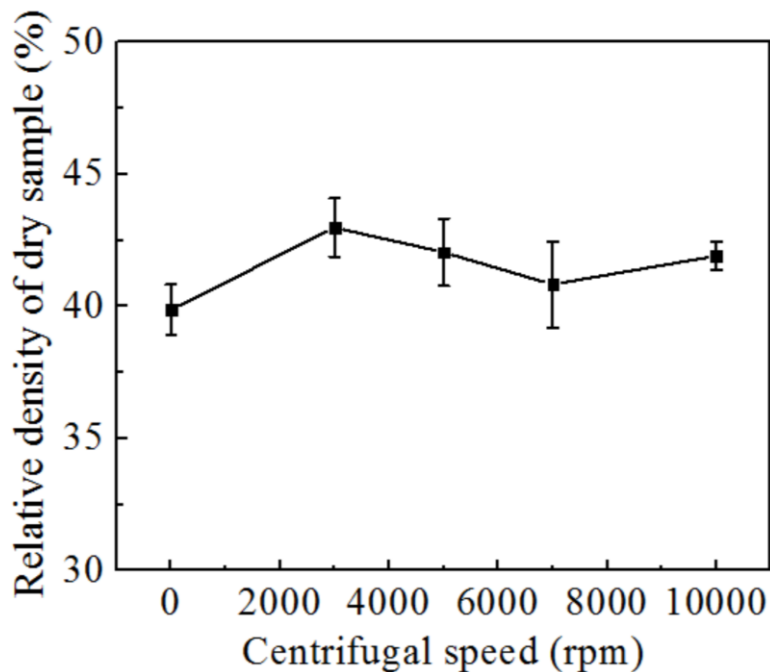
Fig. 2.12. Relative densities of dry ZnO samples prepared at different centrifugal speeds.

During the drying process, the evaporation of the solvent water produces meniscuses at the liquid-vapor interfaces in the pores, which creates capillary compression and drives the internal solvent to flow to the interface. The exterior pressure that drives the shrinkage can be expressed by the following equation [115]:

$$P_E = \frac{2(\gamma_{SV}-\gamma_{SL})}{r} = \frac{2\gamma_{LV}}{r} \tag{1.12}$$

where γ_{SV} and γ_{SL} are the solid-vapor and solid-liquid interfacial energies, respectively, γ_{LV} is the liquid-vapor interfacial energy, r is the radius of the liquid/vapor meniscus. With the shrinkage of the wet ceramic body, the maximum capillary compression P_M can be estimated as [115]:

$$P_M = (\gamma_{SV}-\gamma_{SL})\frac{S_P}{V_P} = \frac{\gamma_{LV}\cos\theta\,S_P}{V_P} = \frac{\gamma_{LV}\cos\theta\,S\rho_b}{1-\rho_R} \tag{1.13}$$

22

where S_P/V_P is the surface-to-volume ratio of the pore space, S is the specific surface area, ρ_b is the density of the dried green body, and ρ_R is the relative density. At the maximum capillary compression, the liquid radius of the meniscus is small enough to fit into the pore, and the ceramic green body stops to shrink. Then the exterior pressure P_E equals the maximum capillary compression P_M. For the ZnO suspension, assuming the interfacial energy of the liquid-vapor water is 0.072 J/m^2 [116], the relationship between the maximum capillary compression P_M and the pore size r is shown in Fig. 2.13a. From the particle size and the relative density of the green body, the average pore size can be estimated to be ~14 nm. Thus, the corresponding average maximum capillary compression P_M during the drying is ~10.3 MPa from Fig. 2.13a. This also means that some pores cannot be removed. In reality, the pore size has a distribution in the green body due to the size distribution of different particles and the agglomeration of some particles. When the pore sizes range from 10-50 nm, the compression on the ceramic body is 14.4-2.88 MPa; the stress in the drying process is nonuniform and can lead to defects. Therefore, it is important to create uniform particle packing during the patterning process and make sure the drying process proceeds homogeneously.
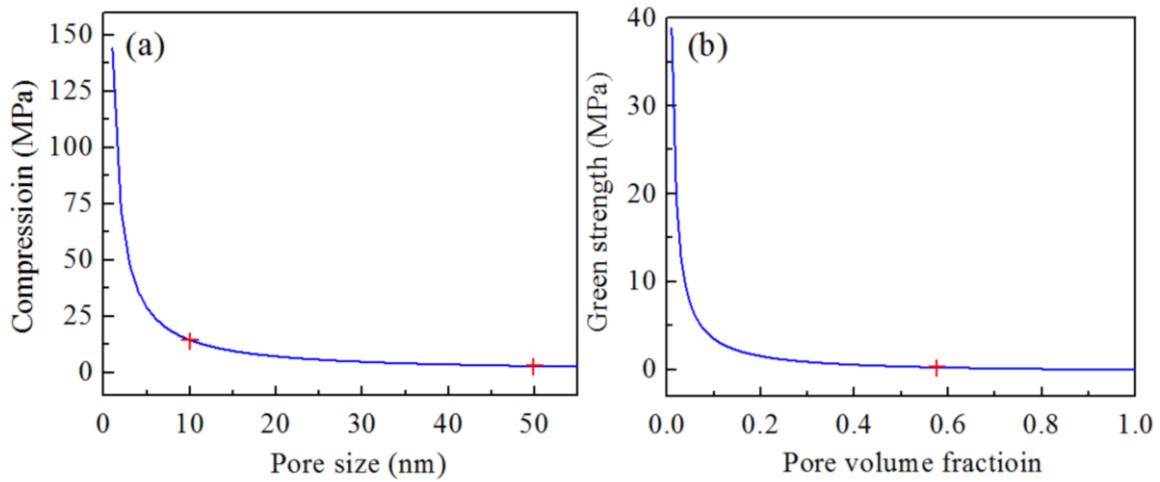
Fig. 2.13. Relationships of compression vs pore size and green strength vs pore volume fraction (The points with cross marks are the calculated values based on the conditions used in our discussion).

Since the wall of the pore consists of particles, the capillary compression pulls the particles together and can densify the samples. The theoretical strength σ of the green body can be estimated as [117]:

$$\sigma = \frac{3\pi}{16}\frac{1-p}{p}S_0\frac{V_b}{V_P} \qquad (1.14)$$

where p is the volume fraction of pores in the body, S_0 is the cohesive or adhesive strength of the binder, the ratio V_b/V_p is related to the weight percent (w) of binder in the body by:

$$\frac{V_b}{V_P} = \frac{w}{100-w}\frac{D_p}{D_b}$$ (1.15)

where D_b and D_p are the densities of the binder and the ceramic particles. Assuming the binder strength is 68.9 MPa [117], the relationship of the green strength σ vs. the pore volume fraction can be plotted as shown in Fig. 2.13b. With the increase of the particle packing density (or with the decrease of the pore volume fraction), the strength of the particle network increases correspondingly. In our prior work on nanoparticle suspension systems [111], the dried nanoparticle packing is 53% relative density; and the green strength is 0.34±0.05 MPa based on a specifically designed green strength measurement technique, close to the prediction of 0.44 MPa in Fig. 2.13b. In the current system, since the same ZnO suspension is used for all the samples, a similar relative density of ~43% is obtained as shown in Fig. 2.12. The pore volume fraction is ~57 vol% and the green body strength is as low as ~0.30 MPa.

During drying, the shrinkage is determined by the particle packing change from the sediment state to the dry state. Fig. 2.14 shows the sediment density (wet sample relative density) and linear shrinkage during drying at different centrifugal speeds. When the centrifugal speeds are 3,000, 5,000, 7,000, and 10,000 rpm, the sediment densities are 33.4%, 34.2%, 34.4%, and 36.2% respectively, and the corresponding linear shrinkages are 4.8%, 5.4%, 6.5%, and 8.1% respectively. With increasing centrifugal speed, higher pressure on the sediment layer leads to denser particle packing at the sediment state. Lower sediment density sample has higher shrinkage and vice versa. The smaller shrinkage for the higher centrifugal speed condition could have also contributed to the higher feature fidelity (smaller LER and larger IC). However, as discussed earlier, when the centrifugal speed is too high, e.g., >7,000 rpm, the deformation of the PDMS mold could set in.
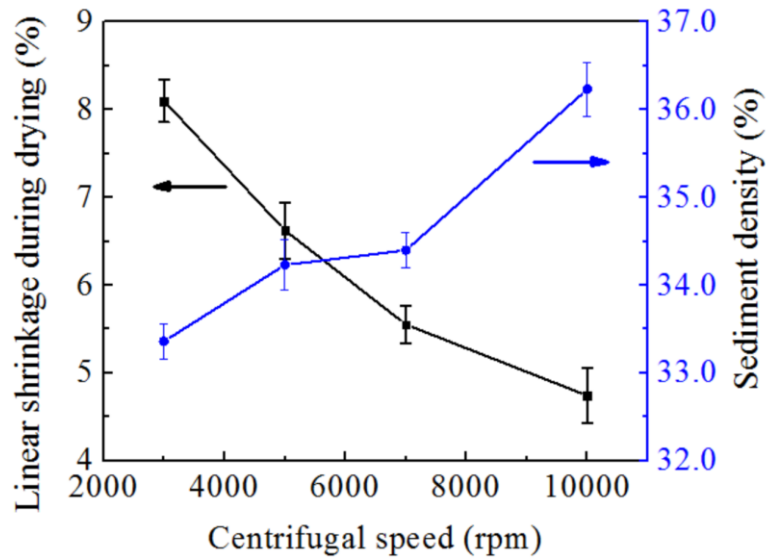
Fig. 2.14. Sediment density (blue) of the ZnO sample prepared at different centrifugal speeds and the corresponding linear shrinkage (black) during drying.

2.3.5 Applicability of centrifuge-aided micromolding to other systems

Since the centrifuge-aided molding process is mainly related to the suspension properties, different nanoparticle suspensions should follow similar processing trends and this study should have wide applicability. The specific feature size limit and patterned feature quality can be estimated. For example, Fig. 2.15 shows the SEM images of ZrO_2 features prepared by the centrifuge-aided micromolding for a similar ZrO_2 suspension (particle size: ~20 nm, solids loading: 25%, viscosity at the shear stress of 64 Pa: ~0.1 Pa·s). The sizes of the obtained ridges are 2.1, 0.9, and 0.4 μm. All the ridges show good fidelity, and the LER values are 4.0±1.1%, 3.5±0.5%, and 3.5±0.8%. For the rods, well-defined round shapes are observed and the average IC value is 0.89±0.02. Since the pattern quality is mainly related to the suspension viscosity (affected by particle size and other suspension properties) and the centrifugal conditions, these results show the generality and wide applicability of the centrifuge-aided micromolding process. The centrifuge-aided molding capability for other nanoparticle suspensions can be similarly predicted and realized.
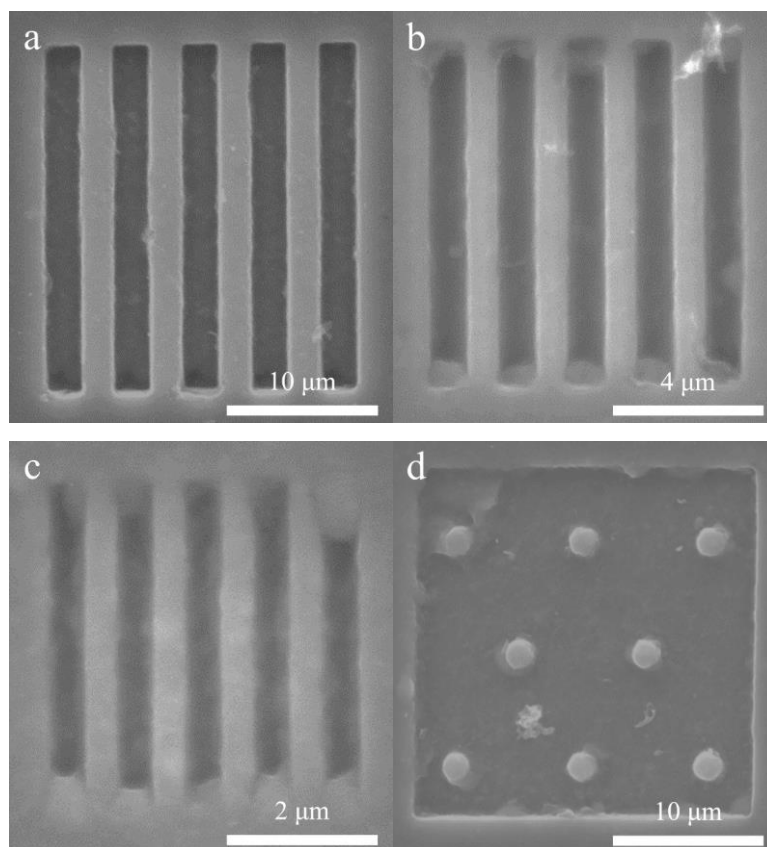
Fig. 2.15. SEM images of ZrO_2 patterns prepared using the same centrifuge-aided micromolding process at 7,000 rpm (a: 2.1 μm ridges, b: 0.9 μm ridges, c: 400 nm ridges, d: 1.9 μm rods).

2.4 Conclusions

Micron- and submicron-sized ZnO patterns are prepared using centrifuge-aided micromolding. Centrifugal force increases the patterning driving force due to the shear-thinning behavior of the ZnO nanoparticle suspension at high solids loading. ZnO nanoparticle-based ridges with sizes from 0.4 μm to 2 μm and rods with a size of 1.6 μm are prepared with good fidelity. The LER values for all the ridges are less than 5% and decrease with the ridge size. The circularity for the rod features is around 0.9, which is close to that of a perfect rod. Centrifugal force reduces the drying shrinkage by increasing the sediment density of the as-cast samples and accelerates the trapped air diffusion rate. Quantitative relationships between the feature size, patterning time, and centrifugal condition are established. The drying process and green body strength are explored. This centrifuge-aided micromolding process can be applicable to many other suspensions, as demonstrated by ZrO_2 nanoparticle suspension patterning.

3 Roughening and Destructive Effects of Sintering on Micron-Sized ZnO Features

3.1 Introduction

Microfabrication has become a critical approach in realizing the miniaturization of devices for diagnostics, microfluidics, and microelectronics [118, 119, 120]. Many advanced techniques have been developed to fabricate micron-sized features, such as capillary molding [12], replica molding [7], and microtransfer molding [10]. Various micron-sized features, namely lines [121], rods/pillars [25, 26], cross- and ring-shaped structures [15], and microwells [122], have been prepared successfully. The micron-sized features can be created not only from soft polymers but also from nanoparticle suspensions. The microfabrication of ZnO [94], Al_2O_3 [123], $PbTiO_3$ [123], and SiC [124] ceramic features by soft lithographic micromolding has been demonstrated.

However, the sintering behaviors of these small features can fundamentally change with size decrease, pose detrimental and unpredictable effects on the manufacturing feasibility of these components/devices, yet have not been examined. During the sintering process, the features will have dramatic morphological and microstructural evolutions because of densification and grain growth. Since sintering is driven by the chemical potential gradient and achieved by the diffusion of atoms via various sintering mechanisms [34], depending on the nature of the material and the sintering condition, one or more sintering mechanisms can play significant roles and lead to drastic microstructure and feature differences.

Many efforts have been devoted to obtaining desired microstructures by controlling the related sintering mechanisms. Chen et. al. utilized a two-step sintering method to obtain fully dense cubic Y_2O_3 with a grain size of 60 nm [44]. Luo et. al. prepared ZnO specimens with relative densities of >97% and grain sizes of ~1 μm via flash sintering [125]. Messing et. al. studied textured piezoelectric ceramics via templated grain growth [126]. An et al realized the control of calcium hexaluminate grain morphology by using different starting calcium-rich powders [76]. Kwon et. al. explored the effect of doping on anisotropic abnormal grain growth of alumina [127]. These studies have demonstrated the critical role of thermodynamics in the sintering behaviors of ceramic materials. However, such understanding has not been extended to micron-sized features.

ZnO has the unique characteristics of the wide bandgap, high exciton binding energy, desired piezoelectric response, and easy doping for applications in electronics, photonics, acoustics, and sensing [81, 128]. The sintering behaviors of bulk ZnO ceramics are well-known and understood [83, 84, 85, 86]. However, for micron-sized features, the sintering behaviors of ZnO

require renewed scrutiny due to the high surface area to volume ratio. The individual grains inside a small feature may grow to the scale of the feature size, and thus exert a huge influence on the feature morphology evolution. So far, only limited studies evaluated the morphology evolution of the sintered features. Kim et. al. investigated the grain size distribution and overall shrinkage of micron-sized ZnO features even though grains grew to the feature size and destroyed the features at late stage sintering [25]. Ye et. al. examined the feature size and grain size for submicron-sized ZnO features. However, polyvinyl alcohol binder content as high as ~50 vol% was used in order to maintain the fidelity of the ZnO features [87]. To obtain a proper understanding of the sintering behavior of micron-sized ceramic features, more focused studies with well-defined features and systematic analysis are needed.

In this study, well-defined and micron-sized ZnO green features are created based on an improved micromolding method with a centrifuge aid. The destruction effects derived from the feature sintering are investigated. Sintering behavior, feature evolution, and surface roughening are explored. Prediction of feature destruction is proposed with respect to sintering time.

3.2 Experimental procedures

3.2.1 Ceramic suspension preparation

ZnO nanopowder (wurtzite structure, 20 nm; Nanostructured Amorphous & Materials Inc., Houston, TX) was used as the starting material. Poly(acrylic acid) (PAA) of 4.5 wt% (Mw 1800; Aldrich Inc., St. Louis, MO) (based on the weight of the ZnO powder) was added as a dispersant and a binder simultaneously. A diluted ammonia solution (pH=11) was utilized as the dispersing medium. A well-dispersed ZnO suspension with a solid loading of ~30 vol% was obtained by a vibratory mill (SPEX 8000 Mixer Mill; SPEX SamplePrep LLC, Metuchen, NJ) after 45 min of mixing.

3.2.2 Ceramic features creation

The casting process was conducted via centrifuge-aided micromolding [129]. First, the as-prepared suspension was transferred into a polydimethylsiloxane (PDMS) mold with as-designed features (2 μm ridges and 4 μm rods). Details of the mold making process can be found in our previous work [94]. Second, the suspension-filled mold was fixed by a self-designed epoxy holder and put into a centrifuge tube. Third, the centrifuge-aided micromolding was carried out at a rotation speed of 7,000 rpm for 30 min (Sorvall Legend X1R, Thermo Fisher Scientific Inc., Waltham, MA). Finally, the PDMS mold with the deposited ZnO layer was

taken out and the solvent on the top was removed. The drying process of ~48 h proceeded in air at room temperature. The dried green ZnO body with features was ultimately separated from the PDMS mold. The sintering process was carried out at 950°C with the heating/cooling rate of 5°C/min in a box furnace (DT-31-FL-10-C front loading, Deltech Inc., Denver, CO). For the samples with ridges, the holding time was kept at 1 min, 10 min, 30 min, 1.5 h, 8 h, and 48 h, respectively. For the samples with rods, the sintering process was carried out at 950°C with the holding time set at 1, 10, 30, 60, and 480 min, respectively.

3.2.3 Characterizations

The relative densities of the sintered ZnO ceramic bodies were measured based on the Archimedes' principle. The sintered ridge features were examined using scanning electron microscopy (SEM, Quanta 600 FEG, FEI Inc., Hillsboro, OR). Line-edge roughness (LER) of the sintered ridges was estimated in order to assess the ridge fidelity [95] by using ImageJ software with the plugin Analyze Stripes. The broken parts of the ridges were not involved in the LER calculation. First, a SEM image was cropped to have the features only. Then the image was converted to greyscale by increasing the contrast, making sure that the ImageJ software evaluated the LER properly. Subsequently, the software established the positions of different feature edges using a fixed reference line and measured the pixel positions of different feature edges. From these data, each edge position and standard deviation of the feature were obtained. The high contrast image allowed the software to detect the feature edge position accurately by identifying the dark-bright pixel changes. The measurements recorded the feature length in pixels, excluding portions of the line where the software could not identify a transition. In this work, the pixels for each LER estimation were no less than 50. Each LER value represented the line-edge roughness as a percentage of the feature size. The circularity value represented the derivation of a featured shape from an ideal round shape, which was used as a gauge for the patterned rod dimensional fidelity. To calculate the circularity value, the area and perimeter of the rod profile from the rod SEM images were obtained first using the Analyze Particles in ImageJ. First, a SEM image was converted to greyscale so that the contrast was heavily increased. Then, the profile of a rod feature was selected using Color Threshold. Finally, the circularity value was obtained by analyzing the selected profile via Analyze Particles function. The equation for the circularity calculation was as follows:

$$Circularity = 4\pi \times \frac{Area}{Perimeter^2} \tag{3.1}$$

3.3 Results and discussion

3.3.1 Ridge degradation observation

Fig. 3.1a shows the SEM images of the green ZnO ridges. The arrangement of the ridges is well defined and the edges of the ridges are straight. The width of the ridges is ~2 μm. Since the ZnO particle size (~20 nm) is much smaller than the ridge size, the morphology of the particles does not show any influence on the fidelity of the ridges. Thus, the ZnO ridges reproduce the shapes and dimensions from the PDMS mold and maintain the high feature quality. Figs. 3.1b-e show the ZnO ridge features sintered at 950°C with different holding time. The sintering process causes the shrinkage of the ridges and grain growth. The shrinkage can be easily seen from the feature area decrease from Fig. 3.1a, to 3.1b, and then to 3.1c. The grain growth is demonstrated by the roughness increase of the ridge surfaces and the ridge edges. With an increase in the holding time, the shrinkage of the feature slows, and the feature area shows no visible decrease. However, the grains in the ridges grow dramatically, leading to rougher ridge edges and deterioration of the ridge fidelity. Specifically, at the holding time of 8 h (Fig. 3.1d), some segments of the ridges become much thinner. With the holding time of 48 h (Fig. 3.1e), the grain size within the ridge is almost equal to the width of the ridge, and just one grain resides in the ridge along the width direction. In addition, some gaps appear between the grains in the ridges and the integrity of the ridges is lost completely. The sintering process destructs the micron-sized ZnO ridges due to grain growth. Because of the wurtzite structure of the ZnO used, some grains in the ridges show hexagonal shapes (as marked in Fig. 3.1e). Because of the preferential growth of the ZnO grains, the exposed surfaces belong to the crystallographic planes with low specific surface energies, such as $(10\bar{1}0)$ (0.84 J/m^2), (0001) (1.68 J/m^2), and $(11\bar{2}0)$ (0.87 J/m^2) [130].
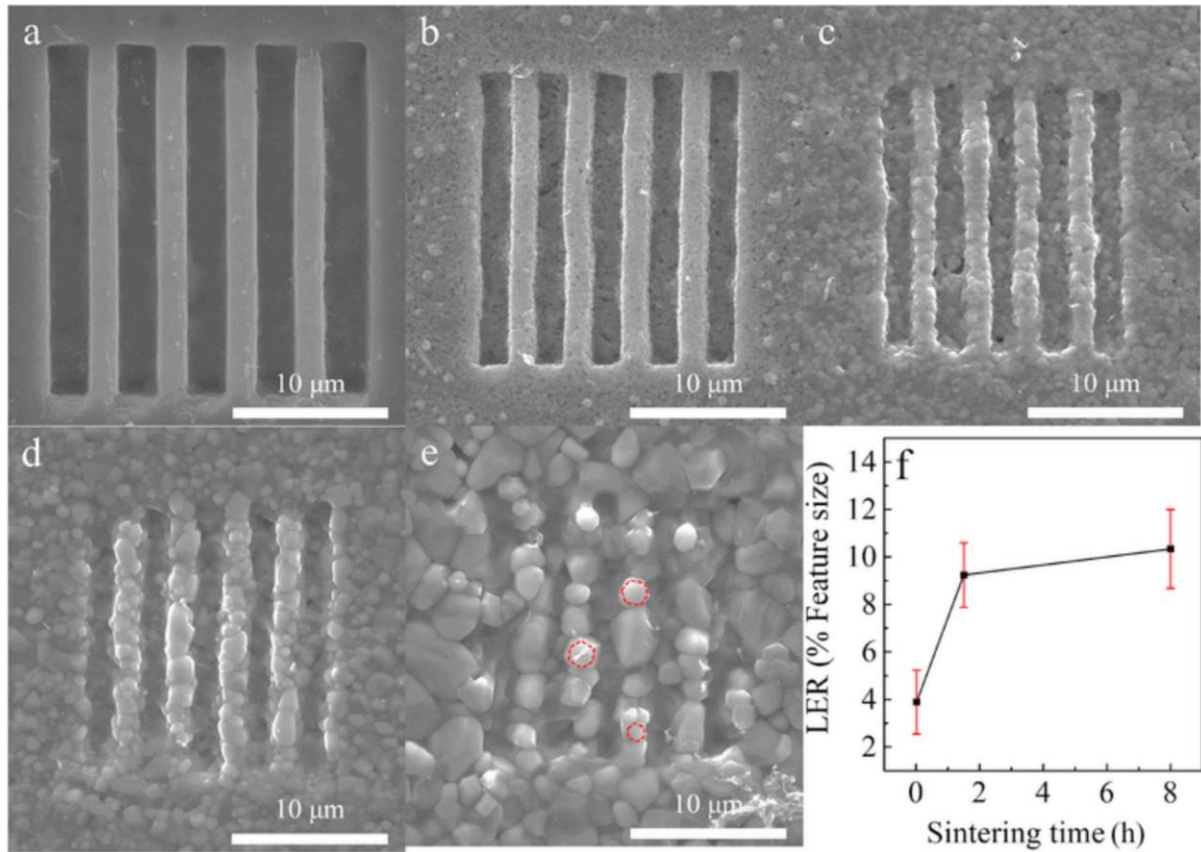
Fig. 3.1. SEM images of ZnO green ridges with 2 μm width (a), ZnO ridges sintered at 950 °C with different holding time of 1 min (b), 1.5 h (c), 8 h (d), 48 h (e), and the corresponding LERs (f).

Fig. 3.1f shows the changes of the LER values for the sintered ZnO ridges with the sintering time. The feature fidelity of the 48 h sintered sample is almost lost (Fig. 3.1e) and the corresponding LER cannot be estimated. Thus, Fig. 3.1f just includes the LERs of the samples with sintering time between 1 min and 8 h. The average LER value at the green state is 2±1%, demonstrating the high fidelity of the ridges. However, the LER value increases dramatically to 9±1% with 1.5 h of sintering, and then to 10±2% with 8 h of sintering. During the sintering process, the ZnO ridge edges tend to become rougher continuously. Nonetheless, the LERs are still acceptable for many applications with the tolerance of the edge roughness within 10% [104, 105, 106].

The evolution of the ridges during sintering is strongly correlated with the densification and grain growth simultaneously. Since the surface of the ridges is comprised of the exposed surfaces of the grains, the ridge morphology and the LER value are affected by the size and shape of the grains. When the grain size is much smaller than the ridge width, the effect from the shape of the grains can be neglected. When the grain size is comparable to the ridge width, the grain shape starts to play a critical role in the ridge shape evolution. It should be mentioned

31

that the ZnO grains are mostly spherical from the initial powder and then become faceted with sintering. In addition, the shrinkage affects the evolution of the ridges in size and morphology.

For the current system, the specific correlation between the ridge roughening/destruction and grain growth can be understood from Fig. 3.2. The grain size in the ridges increases to 0.4, 0.5, 0.9, and 2 μm when the holding time increases to 1 min, 1.5 h, 8 h, and 48 h, respectively. Different from the grain growth, the ridge size first decreases and then increases slightly with sintering, all within the standard deviation with no statistical significance. The corresponding ridge sizes are 1.8, 1.5, 1.6, and 1.7 μm, respectively. This, along with our ongoing work on polymer to ceramic pyrolysis of similar size features, points out an important finding: micron-sized features experience a constraining/self-limiting effect during high temperature thermal processes and cannot shrink. In the meantime, the overall feature area shrinks significantly in the first 1.5 h of sintering and the relative density increases from 55.8% to 95.7% (Fig. 3.2b). During this period, the growth of the ZnO grains has little influence on the ridge size.
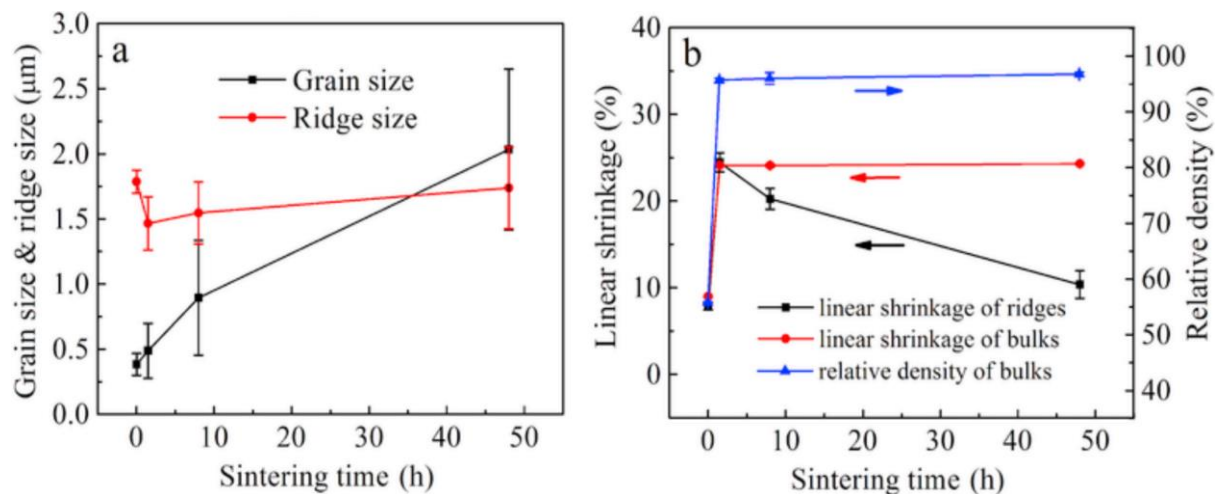
Fig. 3.2. (a) Changes of the ridge grain size and the ridge size at the sintering temperature of 950 °C with different holding time; (b) changes of the linear shrinkage of the ridges and the bulks (primary y-axis) and the bulk relative density (secondary y-axis) at the sintering temperature of 950 °C with different holding time.

The increase of the LER values in Fig. 3.1f can be correlated with the non-uniform dimensional changes of the ridges during sintering. As sintering continues grain growth progresses. When the grain sizes are comparable to the ridge size, the grains start to affect the size and fidelity of the ridges, and the bulk densification has little influence on the feature evolution due to the slow shrinkage rate in the high relative density range (>95%). In addition, the faceting of the ZnO grains leads to abnormal ridge widening, which causes the formation

of gaps along the micron-sized ridges as shown in Fig. 3.1e. This means that the diffusion of the ZnO species during sintering results in the disappearance of some parts of the ridges and the growth of other parts. Destructive sintering effect happens and the ridge size starts to show a surprisingly increasing trend.

Based on Fig. 3.2, the degradation of the ridge fidelity occurs simultaneously with the densification. In this study, the ridge fidelity degradation begins within 1.5 h of sintering holding time. In the same period, the ratio between the grain size and the ridge width increases from 22% to 30%, and the LERs increase from 4% to 9%. This part of the sintering process can be seen as the period when the LER increases dramatically.

Since the sintering destruction process is accompanied by the abnormal dimensional change of the ridges, the starting time of this phenomenon can be estimated by comparing the linear shrinkage difference between the bulk sample and the ridges. Before the abnormal grain growth starts to influence the ridge fidelity (1.5 hrs of sintering), the ridges and the bulk show similar linear shrinkage. When the grain growth starts to affect the ridge fidelity (8 hrs and later sintering), a difference in the linear shrinkages of the ridges and the bulk is created. In the current system, for the sintered sample with 1.5 h of holding time, the linear shrinkages for the bulk and the ridges are both ~25%. This means that the densification effect still plays the major role, and the destructive effect is not obvious. During the following sintering process, for the bulk, the linear shrinkage does not show any obvious increase because of the slow densification rate at the high relative density (>95%). However, for the ridges, an abnormal widening occurs instead of shrinkage. This special phenomenon indicates that grain growth starts to have a major impact on the microstructural evolution of the ridges, and the destructive process becomes significant. Especially, when the grain size is comparable to the ridge width, the grain growth easily leads to the intensive roughness of the ridges and the appearance of gaps in the ridges. After 8 h and 48 h of sintering, the 'apparent' linear shrinkages of the ridges decrease to ~20% and ~10%, respectively. Due to the small size of the ridges, there is not a reliable density measurement technique to compare the feature density and the bulk density difference.

3.3.2 Prediction of ridge destruction

Based on the above observations, grain growth directly leads to the destruction of the sintered ZnO ridges. The ZnO grain size can act as an indicator for the ridge fidelity evolution. According to the result for the ridges with 1.5 h of sintering time, when the grain size reaches 30% of the ridge width (the sintered ridge size reaches 75% of the green ridge size), the grain growth begins to affect the fidelity of the ridges. When the sintering time is increased, the

destructive effect for the ridge feature is enhanced. According to the classical grain growth model, the grain size at a given time can be estimated by:

$$G^n - G_0^n = K_0 t e^{-\frac{Q}{RT}} = Kt \tag{3.1}$$

where G is the grain size at time t, G_0 is the initial grain size (starting particle size), n is the kinetic grain-growth exponent, K_0 is a preexponential constant, Q is the apparent activation energy for grain growth, R is the universal gas constant, T is the sintering temperature, and K is a grain-growth constant at a specific temperature. Since the starting particle size (20 nm) is much smaller than the grain size in the sintered ridges (>400 nm), G_0^n can be neglected. The grain growth can be estimated by:

$$G^n = Kt \tag{3.2}$$

The ridge fidelity destruction time t can be predicted based on the ridge growth adopted from grain growth model of equation (3.2), and expressed as follows:

$$t = \frac{W_s{}^n}{K} \tag{3.3}$$

where W_s is the sintered ridge width. The value of n and K can be determined by regressive fitting based on the experimental data. For the current system, n is 2.01, K is 0.55. According to experimental observation, when W_s reaches 1.5 µm width after 1.5 h sintering, which is 75% of the green ridge size, the destruction start to occur. Therefore, the prediction of the ridge destruction time related to the green ridge size can be plotted as in Fig. 3.3a. The feature destruction time increases with the green feature size. For the 2 µm size green ridges, the approximate destruction time is 4.1 h. So, when the holding time is increased to 8 h, the ridges can be observed with an obvious larger line-edge roughness as shown in Fig. 3.1d than that of the 1.5 h sintered ridges as shown in Fig. 3.1c. When the green ridge size decreases to 1 µm, the destruction time decreases to 1 h, meaning that smaller features are much more vulnerable to destruction during sintering, which can be confirmed from the 1.5 h sintered 1 µm green ridges in Fig. 3.3b. On the other hand, when the green ridge size increases to 4 µm, the sintering time for destruction can be as long as 16.5 h. That is why the 1.5 h sintered 4 µm ridges show near perfect fidelity as shown in Fig. 3.3c, due to the sintering time far away from the predicted destruction time. Based on the estimated destruction time, fidelity change of the ridges during the sintering process can be predicted. If the destruction time is shorter than the needed sintering time, it should be very unlikely to obtain good fidelity after the sample reaches the target relative density. Rather, if the destruction time is longer than the needed sintering time, good fidelity and desired relative density can be expected at the same time.
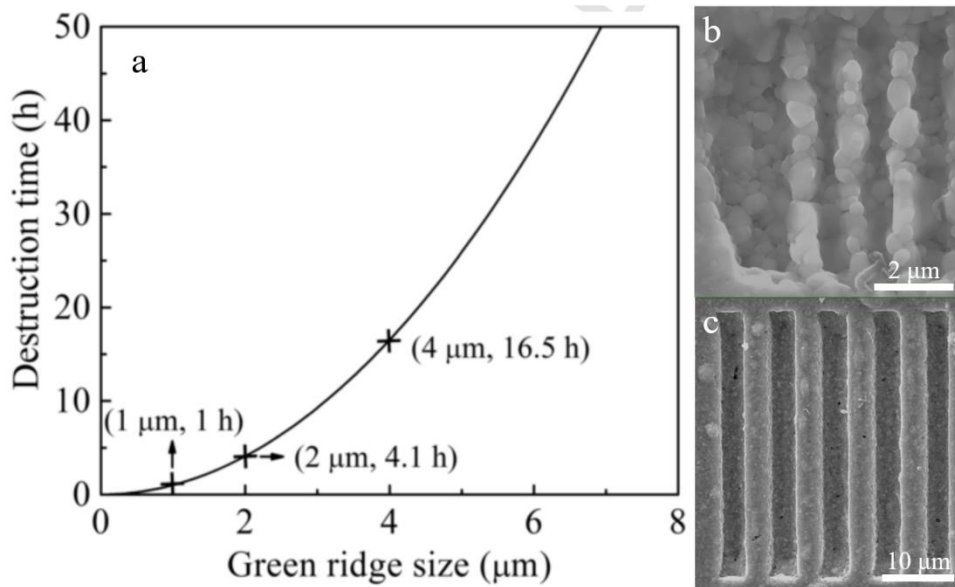
Fig. 3.3. (a) Relationship between the feature destruction time and the green ridge size for ZnO at the sintering temperature of 950 °C (The points with cross marks are the calculated values based on the conditions used in our discussion); ZnO ridge feature with 1 μm (b) and 4 μm (c) width sintered at 950°C with 1.5 hrs holding time.

3.3.3 Rod degradation observation

Fig. 3.4 shows the SEM images of the ZnO rods prepared via centrifuge-aided micromolding before and after sintering. The green ZnO rods in Fig. 3.4a have good fidelity with the average diameter of ~4 μm and an aspect ratio of ~1:2. Each rod possesses a profile close to a perfect circle. Since the size of the ZnO nanoparticles (~20 nm) is much smaller than the rod diameter, the morphology of the particles does not have an obvious influence on the fidelity of the rods, as shown from a rod with a magnified image in Fig. 3.4a. With the centrifugal aided casting approach, the ZnO rods can be made near perfectly from the PDMS mold and maintain high feature quality.
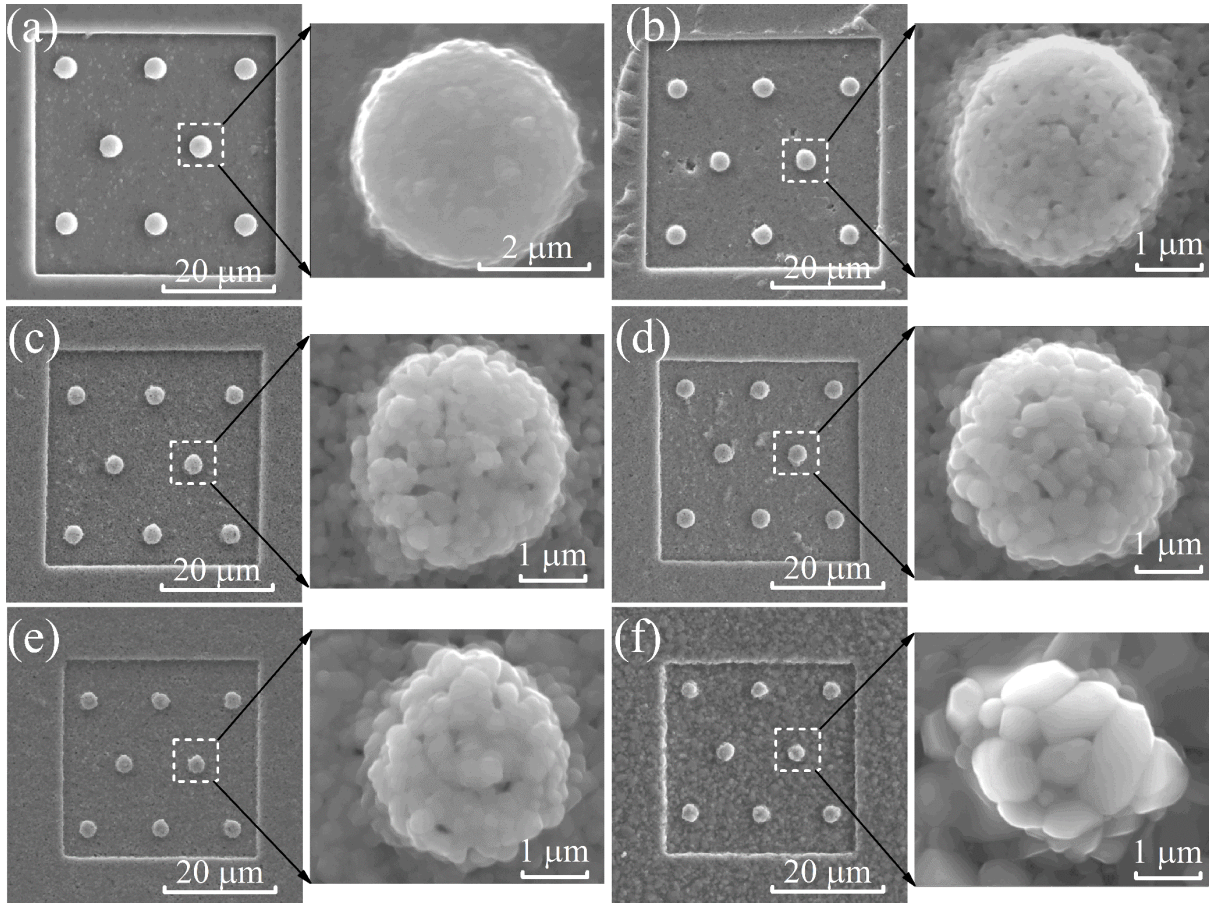
Fig. 3.4. SEM images of green ZnO rods (a) and sintered ZnO rods with holding time of 1 min (b), 10 min (c), 30 min (d), 60 min (e), and 480 min (f) at 950°C.

Figs. 3.4b-f show the ZnO rods sintered at 950°C with different holding time. The morphology change and the grain growth with the holding time can be easily seen. The sintering results in the shrinkage of the rod patterns and the rod sizes. With the increase of the holding time, the rod pattern shrinks gradually, and the surface becomes rougher due to grain growth. When the holding time reaches 480 min, the grains have very large sizes and the rod shape is severely distorted from the round shape. This phenomenon will affect the usability of the structure and the properties of related devices.

Based on the SEM images in Fig. 3.4, the circularity of the rods at different holding time is shown in Fig. 3.5. Before sintering, the circularity for the green rods reaches 0.90, very close to 1, meaning an almost perfect circle shape. After sintering with the holding time at 1, 10, 30, 60, and 480 min, the corresponding circularity values are reduced steadily to 0.84, 0.83, 0.78, 0.76, and 0.64, respectively. Longer sintering time leads to more significant circularity loss. For example, the circularity of the 1 min sintered rods is just 6% smaller than that of the green rods, whereas the circularity of the 480 min sintered rods is 26% less than that of the green rods. As seen from Fig. 3.4, the decreases in the rod circularity and the rod fidelity are

strongly associated with grain growth. Besides, with the wurtzite structure of ZnO, the grains tend to expose the low energy crystalline planes (such as $(10\bar{1}0)$ [130]) more easily, and are likely to produce relatively sharp edges/corners on the sintered rod surfaces.

Time (min)	Circularity
0	0.90
1	0.84
10	0.83
30	0.78
60	0.76
480	0.64
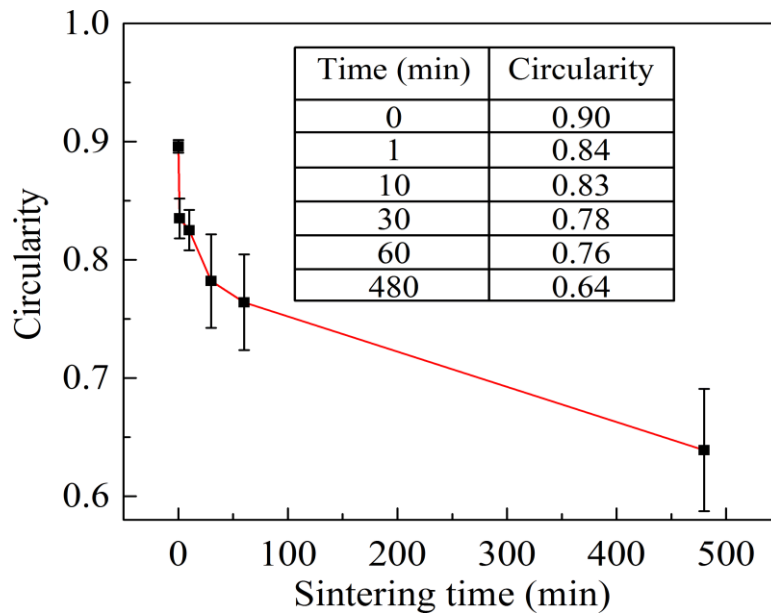
Fig. 3.5. Change of circularity values with the sintering holding time.

Fig. 3.6 shows the linear shrinkages of the ZnO rods and the bulk with different holding time. When the holding times are 1, 10, 30, 60, and 480 min, the corresponding linear shrinkages of the rods are 17.8±1.1%, 20.2±1.7%, 22.6±0.7%, 26.2±1.0%, and 27.2±4.6%, respectively; the corresponding linear shrinkages of the bulk are 13.6±0.5%, 19.3±0.3%, 22.0±0.9%, 23.5±0.4%, and 24.8±0.5%, respectively. Both the rods and the bulk show fast shrinkage within the initial 60 min of the sintering time, and stabilize with longer sintering time after that. However, the rods always demonstrate a higher shrinkage than that of the bulk at the same sintering time. It means that the features have higher densification rates than the bulks.
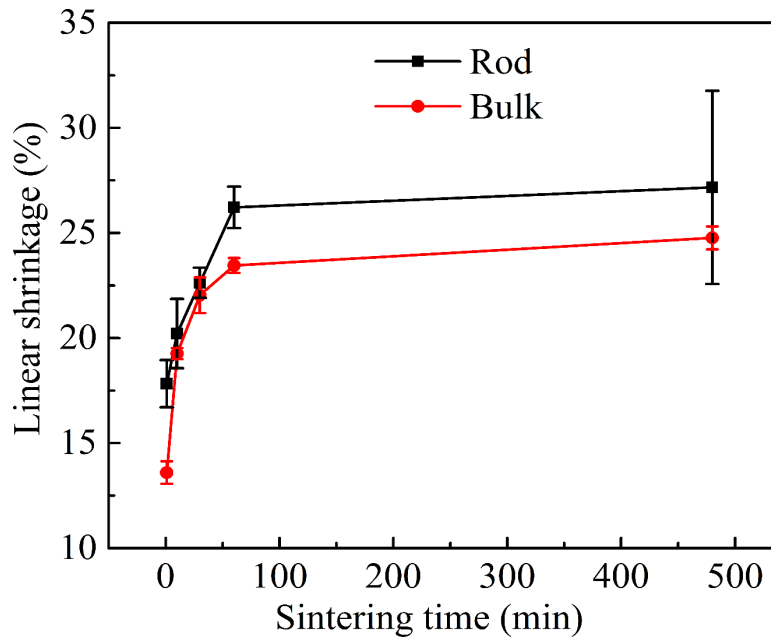
Fig. 3.6. Linear shrinkage of the rods and the bulk with sintering time.

Fig. 3.7 shows the relative density of the ZnO bulk with different sintering time. When the holding times are 1, 10, 30, 60, and 480 min, the corresponding relative densities are $55.8\pm0.1\%$, $56.3\pm0.1\%$, $77.0\pm0.1\%$, $89.8\pm0.1\%$, and $96.8\pm0.3\%$, respectively. Drastic density increase occurs in the first 60 min of sintering. The trend in the relative density change for the bulk is the same as that of the shrinkage since the shrinkage is directly related to the relative density. Fig. 3.7 also shows the grain sizes in the ZnO rods and bulks with different holding time. When the holding times are 1, 10, 30, 60, and 480 min, the corresponding average grain sizes in the bulk samples are 0.17 ± 0.07, 0.24 ± 0.05, 0.55 ± 0.31, 0.74 ± 0.36 and 2.38 ± 2.05 µm, respectively, and the corresponding average grain sizes in the rods are 0.15 ± 0.04, 0.17 ± 0.05, 0.23 ± 0.07, 0.30 ± 0.10 and 0.69 ± 0.21 µm, respectively. The increasing relative density and grain size for the ZnO bulk means that the densification is accompanied by grain growth during the sintering process, as widely understood. The grain growth in the rods has the same increasing trend as that of the bulk, but the grain size is smaller. Not surprisingly, the grain growth leads to the deformation of the rod profile (Fig. 3.4) and thus compromises the rod circularity (Fig. 3.5).
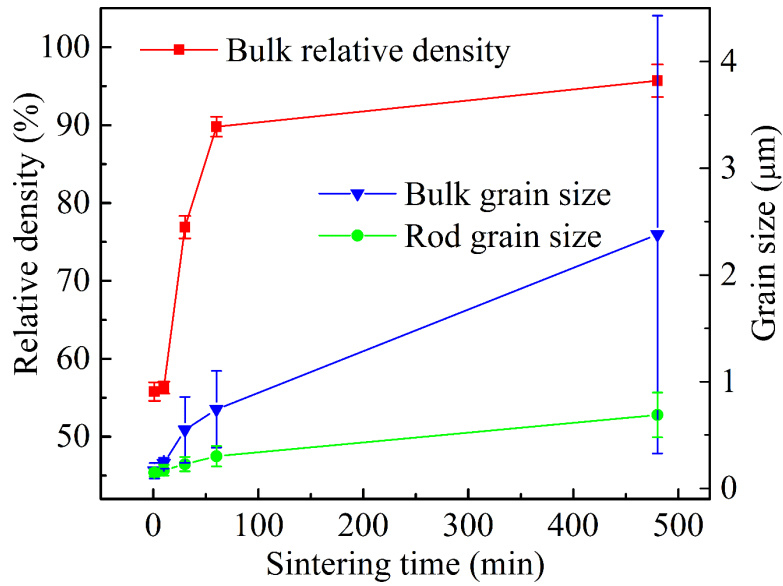
Fig. 3.7. Bulk relative density, bulk grain size, and rod grain size with different sintering time.

3.3.4   Thermodynamic analysis of feature surface roughening

Based on the Kelvin equation, considering the geometric factor only, a surface with negative curvature (concave) has a lower chemical potential than a flat or convex surface. The chemical potential difference leads to a flux of atoms from a flat or convex surface to a concave surface, which causes the flattening of both the concave surface and the convex surface. For the ZnO system, the small/sharp locations on the ridges will shrink and the large/round locations will grow during sintering. From the specific surface energy point of view, a surface with a higher specific surface energy has higher chemical potential. The chemical potential difference leads to a flux of atoms along the direction of decreasing specific surface energy and expands the surface region with lower specific surface energy. Crystallographic planes with a lower specific surface energy will preferentially grow to form a polyhedron with sharp edges. For an actual system, these two factors work simultaneously and the sintering behavior can be seen as a result of the competing effects due to the diffusion of the involving species. Eventually, the ridge loses its original shape, and surface roughening occurs. For the micron-sized ZnO ridges, when the grain size is comparable to a ridge size, the ratio of the grain boundary area to the surface area becomes very small. Theoretically, based on the model of closely packed spheres, when the ratio of the grain size to the ridge size increases from 0.5 to 1, the ratio of the grain boundary area to the surface area will decrease from 3 to 1. Thus, evaporation, surface re-condensation, and surface diffusion will modify the feature surface

39

morphology during the sintering process. The feature surface morphology evolution can be estimated by balancing the chemical potentials.

As illustrated in Fig. 3.8, the tri-junction regions at two adjacent grains usually have a higher surface energy compared to the free surface due to the relatively disordered arrangement of atoms near the grain boundary, which increases the chemical potential [131, 132, 133]. Meanwhile, these tri-junction regions usually have negative curvatures. Thus, the geometry and specific surface energy difference at these locations have opposite effects on the chemical potential, which drives the movement of diffusing species. When these two fluxes are equal, the net flux should be zero and the tri-junction region will reach a stable state.
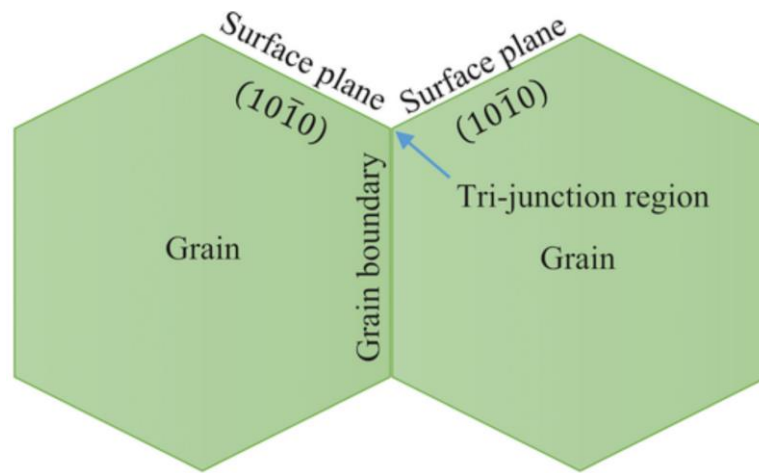
Fig. 3.8. Illustration of the tri-junction region using the $(10\bar{1}0)$ plane of ZnO as an example.

In order to simplify the problem, an ideal model can be proposed: the tri-junction region has a symmetric structure along the grain boundary, and the grain surfaces on both sides belong to the same family of crystal planes (see the illustration in Fig. 3.8). According to the Young-Laplace equation, the change of chemical potential $\Delta\mu_c$ from the curvature of the surface can be expressed by:

$$\Delta\mu_c = 2\gamma_s \frac{\Omega}{R_s} \tag{3.4}$$

where γ_s is the specific surface energy, Ω is the molar volume, and R_s is the curvature radius of the surface. The change of chemical potential $\Delta\mu_s$ from the difference in specific surface energy and grain boundary energy can be expressed by:

$$\Delta\mu_s = \Delta\gamma_s S_A = \Delta\gamma_s \frac{\Omega}{d} \tag{3.5}$$

where $\Delta\gamma_s$ is the specific surface energy difference, S_A is the surface area occupied by one mole of ZnO, and d is the atomic plane spacing. The equilibrium condition can be expressed as:

$$\Delta\mu_c = \frac{2\gamma_{sp}}{R_s} = \Delta\mu_s = \frac{(\gamma_{sg} - \gamma_{sp})}{d} \tag{3.6}$$

where γ_{sg} is the specific energy of the grain boundary and γ_{sp} is the specific surface energy of the grain surface. Assuming the curvature gradient and specific surface energy gradient are constant across the tri-junction region, the curvature radius of the region can be estimated by equation (3.6):

$$R_s = \frac{2\gamma_{sp}d}{\gamma_{sg}-\gamma_{sp}} \tag{3.7}$$

In the current system, γ_{sg} is 1.77 J/m^2 [134], γ_{sp} can be estimated using the specific surface energy of a crystallographic plane. Usually, the exposed crystallographic planes with low specific surface energies are $(10\bar{1}0)$(0.84 J/m^2) (commonly exposed plane), (0001)(1.68 J/m^2), and $(11\bar{2}0)$ (0.87 J/m^2) [130]. The corresponding values of lattice d spacing are ~0.14, 0.22, and 0.24 nm, respectively [135]. Based on equation (3.7), the corresponding radius R_s is 0.53, 8.65, and 0.94 nm, respectively. This means that a tri-junction region with a curvature radius from several to dozens of nanometers will be obtained when the chemical potentials become equal. So, the lower the specific surface energy is, the smaller the curvature radius of the tri-junction region is. The crystallographic plane with the lowest specific surface energy is most likely to be the exposed grain surface. The formation of this sharp tri-junction region should be a general phenomenon for any particle-based sintering system, as shown in Fig. 3.1e. Since this process is driven by the chemical potential difference, the decrease of the curvature radius will last until the balance is reached. The formation of the tri-junction region with a small curvature radius is realized by the movement of the atoms from the grain boundary region to the feature surface. When the centers of the two grains along the ridge are too far apart, the continuous loss of species at the grain boundary region will create a gap between the grains.

It should be mentioned that the above analysis is based on an idealized situation; the obtained values for R_s are not exact values. In a realistic situation, the orientations of the grains are random, and so are the crystallographic planes on both sides. Although these factors make it difficult to predict the exact curvature radius, the trend to form a sharp tri-junction region should be the same if evaporation, surface re-condensation, and surface diffusion become significant during the long time sintering process. The tri-junction regions are the most vulnerable locations to form a sharp angle, which increases the LER values. When the distance between the grains is large enough, there will be a feature break-up tendency, e.g., by forming gaps along the ridge length direction.

Based on the above discussion, several strategies can be utilized to limit the feature destruction effect. First, since grain growth is the direct reason of feature breaking, strategies that can limit grain growth should be effective, such as two-step sintering [44], microwave

sintering [136], and grain growth inhibitor doping [137, 138, 139]. For two-step sintering, the relatively low holding temperature can limit grain growth effectively. The fast heating of microwave can also limit the grains from growing too fast. Grain growth inhibitors can stay at grain boundaries to hinder grain boundary migration and thus grain growth. Second, for the ZnO system, the evaporation mechanism is usually activated at ~900 ℃, lower sintering temperature can limit this mechanism and the corresponding feature breaking process [83]. Finally, feature shapes and sizes will also affect the destructive effect. Obviously, large size features can sustain longer sintering time. For ridges, the two ends connected to the bulk can slow down the grain growth to a certain extent.

3.4 Conclusions

This study focuses on the sintering behavior of micron-sized ZnO features. Feature destruction occurs due to the abnormal grain growth. Feature destruction time and the corresponding relative density are predicted based on developed models. Surface roughening process is further explained based on the chemical potential difference between grain surface and grain boundary, which is correlated to the evaporation, surface re-condensation, and surface diffusion. This work provides the first guidance on predicting and controlling the sintering behaviors of micron-sized features.

4 Effects of Atmosphere on Evolution of Micron-sized ZnO during Sintering

4.1 Introduction

In recent years, many microfabrication techniques have been developed to fabricate micron-sized features for miniaturization and portability of devices, such as photolithography [2], soft lithography [1], photomasking [4], focused ion beam milling [3], and electron beam lithography [5]. Many materials have been used to fabricate various micron- and nano-sized features, such as polymer [140, 141], metal [20], and ceramic materials [78].

For ceramic micron-sized feature fabrication, sintering plays a critical role in shape retention and microstructural evolution [25, 87, 142]. Different from bulk ceramic sintering, the sintering behaviors of these features can fundamentally change with the decrease of their sizes. The most direct influence is the limitation imposed by grain growth. For the grains in the feature, their sizes cannot exceed the feature size. However, densification inevitably incurs grain growth. When grain growth is limited to single micron size or lower, the densification of micron-sized ceramic features will be affected; sometimes it is impossible to densify the features to the desired densities, as externally applied sintering driving force is not feasible, which presents a problem different from that of the bulk ceramics. In addition, with continuous sintering, the features will have dramatic morphological and microstructural evolutions. Constrained shrinkage may distort the original shape. When the grain size is comparable to the feature size, the influence of individual grains cannot be neglected. The changes in the shape and size of grains can completely alter the designed features. As a result, unpredictable effects on the manufacturing feasibility of these components/devices may happen.

ZnO exhibits special properties in chemistry, surface, and microstructure and has wide applications as varistors [143], gas sensors [144], transparent electrodes [145], and catalyst [146]. Many sintering researches have been done to understand the relationship between sintering process and microstructural evolution [83, 85, 86, 147, 148, 149, 150, 151, 152]. Gupta and Coble studied the grain growth expression of pure ZnO from a phenomenal kinetic view [151, 152]. Ewsuk et. al. demonstrated that grain boundary diffusion is the single dominant sintering mechanism in the intermediate sintering state of nanocrystallineand ZnO [85]. Besides, one special feature for this material is the high vapor pressure (~2 kPa at 1000 ºC) [153], compared to other ceramic material, such as alumina (~100 Pa at 2100 ºC) [154]. Hynes et. al. proved that a higher specific surface energy may contribute to a faster densification rate and the mass transport via vapor phase will

increase above 950 °C [83]. Meanwhile, the sintering atmosphere may affect the surface composition of the particles, and the changed surface chemical potential will affect mass transport via various sintering mechanisms. Although exiting results were obtained by these researchers, almost all these efforts are about bulk samples. For micron- or submicron-sized ZnO features, we have demonstrated that the change in shape and size of grains during sintering directly affects the morphology evolution of the features. When the grain size grows to 30% of the feature size, the subsequent grain growth will deteriorate or even destroy the fidelity of micron-sized ZnO ridges [155]. In addition, with different atmospheres, the partial pressure of ZnO can change and act as another factor in influencing the small feature sintering behaviors. For example, the evaporation-condensation rate can be accelerated or decelerated [153, 156]. Besides, compared to bulk, the evaporation effect of ZnO on the features can become much more significant [157]. Especially in the final sintering stage, the evaporation effect on the features will be much more significant due to the much larger specific surface area in comparison with the bulk [158]. Previously, with working the ZnO bulk, researchers put less attention to the role of the evaporation effect in the densification process. However, for small ZnO features, the evaporation effect will play a more important role, and both the sintering process and morphology evolution will be affected obviously [159]. It means that new sintering models and math expression considering evaporation factor should be established to illustrate the role and effect of sintering atmospheres.

In this work, micron-sized ZnO ridges were sintered in different atmospheres. The evolution of the ZnO ridges was characterized by measuring the ridge size and grain size. The microstructure of the sintered ridges is visualized by 3D reconstruction. The effect of atmospheres on sintering was studied by analyzing the difference in the ridge integrity and microstructural evolution. Fundamental theories were established to explain the evolution of such microstructures.

4.2 Experimental procedures

4.2.1 Ceramic suspension preparation

ZnO nanoparticles (~20 nm; wurtzite structure; Nanostructured and Amorphous Materials, Inc., Houston, TX) were used to fabricate the micron-sized ZnO ridges via centrifuge-aided micromolding based on our previous work [160]. 4.5 wt% poly (acrylic acid) (PAA) (Mw 1800; Aldrich, St. Louis, MO, based on the weight of ZnO powder) was used as a dispersant and a binder simultaneously. A diluted ammonia solution with a pH value of 11 was used as the dispersing medium. A well-dispersed ZnO suspension with a solid loading of ~30

vol% was obtained via a vibratory mill (SPEX 8000 Mixer Mill; SPEX SamplePrep LLC, Metuchen, NJ) after 45 mins of mixing.

4.2.2 Ceramic features creation

The casting process was implemented via centrifuge-aided micromolding. First, the suspension was transferred into a PDMS mold with 2 μm ridge patterns. Second, the suspension-filled mold was fixed in a centrifuge tube by a self-designed epoxy holder. Third, the centrifuge-aided micromolding was conducted at a rotational speed of 7000 rpm for 30 min. Finally, the PDMS mold with the deposited ZnO nanoparticle layer was taken out and the extra solvent on the top was removed. The drying process of ~2 days proceeded in the air at room temperature. The dried ZnO green body with the 2 μm ridges was ultimately demolded from the PDMS mold. The atmosphere sintering process was carried out at 1000 °C with different holding time and the same heating and cooling rate of 5 °C/min in a box furnace (DT-31-FL-10-C front loading, Deltech, Denver, CO). High purity argon (purity: 99.999%, oxygen content: ~1 ppm, Airgas, Christiansburg, VA) and dry air (oxygen content: ~21%, Airgas, Christiansburg, VA) were used as the sintering atmospheres and the corresponding partial pressures of oxygen were 0.0001 and 21.1 kPa, respectively.

4.2.3 3D reconstruction

The microstructures of the sintered ZnO samples were characterized by FIB-SEM 3D analysis using a dual beam FIB microscope (FEI Helios 600 NanoLab, Hillsboro, OR). Before the FIB cutting, the sample was coated with a gold layer (~10 nm) using a sputter coater (208HR High Sputter Coater, Cressington Scientific Instruments Ltd., Watford, England). After the sample was placed inside the FIB microscope, a 1 μm circular Pt layer was deposited on the target ZnO feature in order to provide more conductivity, which should also avoid the milling of the ZnO surface structure and waterfall artifact during the FIB cutting. The electron beam current was 22 nA, and it took around 4 min to deposit the Pt layer. Before serial cutting, several cleaning cuttings with an interval of 50 nm were done using 93 pA current under 30 kV voltage.

After all the preparation was done, the cross-section of the ZnO rod was cut off layer by layer with a spacing of 10 nm using 93 pA current under 30 kV voltage, and an SEM image was taken under optimal contrast and brightness after each slice was removed. A good contrast was critical for the image digitization and 3D reconstruction. 30 slices were collected from the middle part of the feature.

The 3D reconstruction was realized using the software Amira 5.4.1 (Visage Imaging, Inc., San Diego, CA). First, after loaded into the software, the slice images were aligned roughly by the AlignSlice module. All the areas outside the area of interest (the ZnO ridge) were cropped out. The selection of different microstructure components (grains and pores) was completed in Segmentation mode. In order to improve the accuracy of the selection, the procedure was completed manually. Then, grains and pores were labeled and colored separately. A 3D model consisting of all the labeled microstructure components was shown by using SurfaceGen command. Quantitative 3D microstructural data, including the volume of each component, was extracted based on the 3D model. More information, including relative density, was obtained based on the extracted data via a basic calculation.

4.2.4 Characterization

The relative densities of the green and sintered ZnO bodies were measured based on the Archimedes' principle. The morphology of the sintered ridges was examined by scanning electron microscopy (SEM, Quanta 600 FEG; FEI Company, Hillsboro, OR). Line-edge roughness (LER) of the sintered ridges was estimated in order to assess the ridge fidelity [95] by using ImageJ software with the plugin Analyze Stripes. The broken parts of the ridges were not involved in the LER calculation. First, a SEM image was cropped so that only the features were visible. Then the image was converted to greyscale and the contrast was heavily increased. The software established the position of each line based on the greyscale values and measured the distance in pixels between two lines. From the data, the ridge width and standard deviation of that measurement were isolated. The LER values represented the line-edge roughness as a percentage of the feature size.

4.3 Results and Discussion

4.3.1 Sintering of ZnO bulk

The sintering atmosphere has a continuous influence on the densification of the bulk ZnO ceramic. Fig. 4.1 shows the relative densities of the ZnO samples sintered in argon and air atmospheres at $1000^{\circ}C$. When the sintering time is kept at 1, 90, and 480 min, the relative density of the ZnO bulk sintered in argon are $66.30\pm1.67\%$, $86.36\pm0.68\%$ and $92.37\pm1.06\%$, respectively, and the relative density of the ZnO bulk sintered in air atmosphere is $65.90\pm0.76\%$, $79.12\pm1.65\%$ and $89.87\pm1.58\%$, respectively. With the short sintering time of 1 min, their relative densities are very similar, and the sintering atmosphere does not affect the densification obviously. When the sintering proceeds to longer holding time, the difference in the relative

density becomes more obvious. The argon atmosphere accelerates the densification of the bulk ZnO in comparison with the air atmosphere.
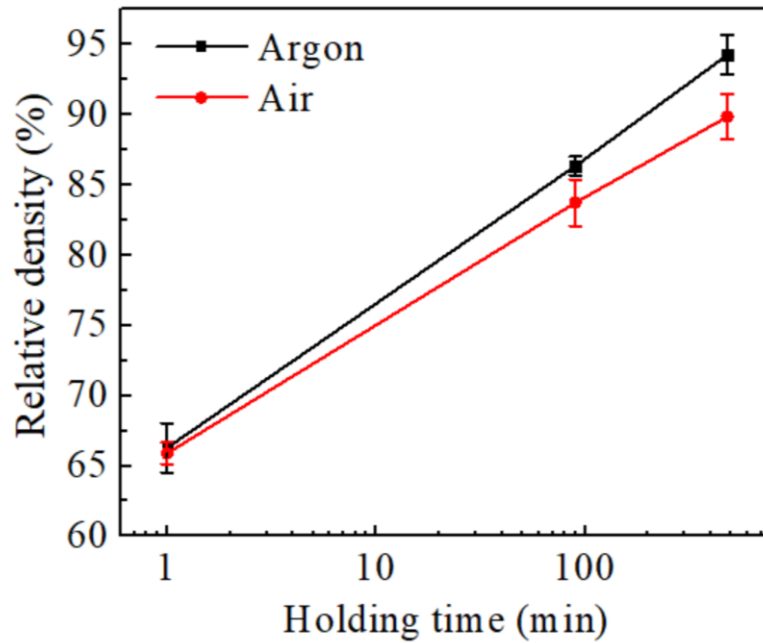
Fig. 4.1. Relative densities of the sintered bulk ZnO samples with argon and air atmospheres at 1000°C.

During the ZnO sintering process, ZnO decomposition and defects formation will matter greatly for densification and grain growth [161]. On one aspect, the decomposition can not only lead to the evaporation and roughen the surface, but also trigger the zinc interstitial defects. One other aspect, thermodynamics also produces the defects automatically, which has been confirmed to be mainly the oxygen vacancy [162, 163]. The oxygen vacancies tend to have the larger diffusion speed than that of zinc interstitials due to the lighter mass of oxygen atom than that of the heavier mass of zinc atom. Therefore, the lower diffused zinc interstitials finally determine the mass transportation and contribute the densification during the ceramics sintering process [164]. In this work, the evaporation effect from the ZnO decomposition as well as the induced Zn interstitial diffusion will be considered for the explanation of the sintering behavior difference between ZnO bulk and ridges. The chemical reaction of ZnO decomposition and the defect reaction of Zn interstitial formation can be expressed as follows:

$$ZnO(s) \leftrightharpoons Zn(g) + \frac{1}{2}O_2(g) \tag{4.1}$$

$$Zn(g) \leftrightharpoons Zn_i^{\cdot} + e' \tag{4.2}$$

When the equilibrium states are achieved for reactions (4.1) and (4.2), the corresponding equilibrium constants K_1 and K_2 can be obtained as follows [161]:

$$K_1 = P_{Zn}P_{O_2}^{\frac{1}{2}} \tag{4.3}$$

47

$$K_2 = [Zn_i^{\cdot}][e'][P_{Zn}]^{-1} \tag{4.4}$$

where, P_{Zn} is the partial pressure from the Zn gas, P_{O_2} is the partial pressure from O₂ gas, $[Zn_i]$ is the concentration of Zn interstitials, $[e']$ is the concentration of electrons. With the combination of equations (4.3) and (4.4), the $[Zn_i]$ concentration can be obtained as:

$$[Zn_i] = \sqrt{K_1 K_2}\, P_{O_2}^{-\frac{1}{4}} \tag{4.5}$$

The densification processes in Fig. 4.1 show typical semilogarithmic relationships, which can be expressed as [166]:

$$\frac{d\rho}{dt} = \frac{K}{t} \tag{4.6}$$

where ρ is the density and K is the constant. K has the expression:

$$K = \frac{A D_{Zn}\, \gamma_{sv}\, \Omega}{\alpha k T} \tag{4.7}$$

where A and α are constants, D_{Zn} is diffusion coefficient of Zn interstitial (2.44×10^{-11} m²/s) which are obtained by curve fitting and calculation, γ_{sv} is the surface energy of solid/vapor, Ω is atomic volume of Zn interstitial (1.41×10^{-31} m³), k is the Boltzmann constant (1.381×10^{-23} J·K⁻¹), T is the absolute temperature (1273 K). The value of K can be determined by measuring the slope of ρ vs $\log(t)$ in the sintering process.

After integration of equation (4.6), it can be expressed as:

$$\rho = \rho_0 + K \mathrm{Ln}(t) \tag{4.8}$$

where ρ is the density, ρ_0 is the initial density. If both sides are divided by the theoretical density of ZnO with ρ*, equation (4.8) can be changed to:

$$D = D_0 + K^* \mathrm{Ln}(t) \tag{4.9}$$

where $D = \rho/\rho^*$, which is the relative density; $D_0 = \rho_0/\rho^*$, which is initial relative density; $K^* = K/\rho^*$. Now, based on the plot in Fig. 4.1 of the relative density and time, the parameter K^* of the bulk ZnO ceramic sintered in different atmospheres of air and Ar can be obtained by curve fitting.

Based on the above equations, it can be found that only surface energy can be affected by the change of the defects concentration on the surface. It is assumed that the sintering atmosphere affects the densification rate by changing the surface energy. In air atmosphere, the surface energy is ~2.8 J/m². By comparing the densification rate in argon and air, the surface energy in argon atmosphere can be estimated, which is ~4.2 J/m² [167].

4.3.2 Sintering of ZnO ridges

The sintering atmosphere affects the morphology evolution of the ZnO ridges during sintering. Fig. 4.2 shows the ZnO ridges sintered in air and argon atmospheres at 1000°C. The

ridges sintered in both air and argon experience obvious shrinkage. Compared to the ZnO ridges sintered in air, the ridges sintered in argon show more and faster feature fidelity loss. Especially, when the sintering time increases to 8 hrs, the ridges sintered in argon even lose continuity. The argon atmosphere has a more destructive effect on the micron-sized ZnO features. The grains also grow differently for the Ar and air sintered samples. The Ar sintered samples show faster grain growth compared to the Air sintered samples.
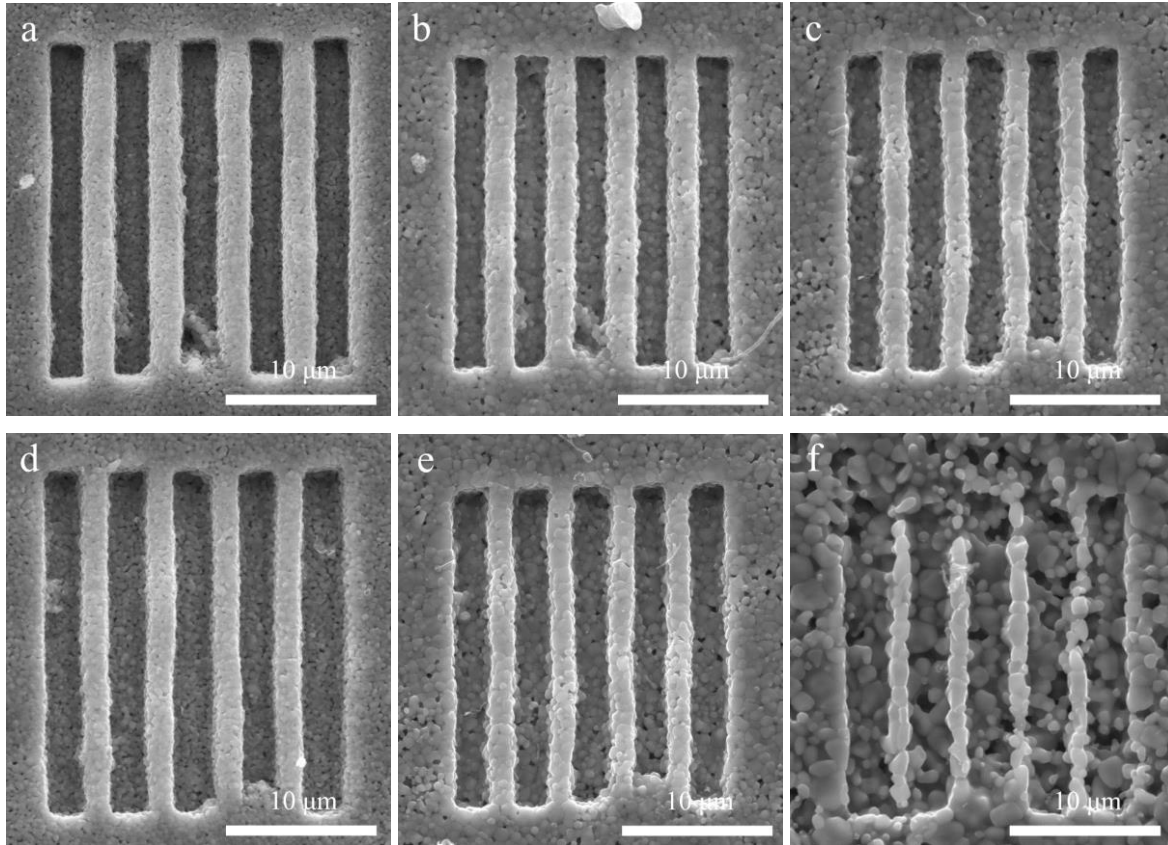
Fig. 4.2. SEM images of the sintered ZnO with 1 min sintering time in air (a) and Ar (d), 1.5 hrs sintering time in air (b) and Ar (e) and 8 hrs sintering time in air (c) and Ar (f).

The effect of the sintering atmospheres on the feature fidelity can be characterized quantitatively from two aspects: ridge width and line edge roughness. Fig. 4.3a shows the LER values of the ZnO ridges sintered under different conditions. When the sintering time is 1, 90, and 480 min, the LER values of the ZnO ridges sintered in Ar are 2.60±0.44%, 4.57±1.01% and 6.71±1.71%, respectively, and the LER values of the ZnO ridges sintered in air are 2.46±0.92%, 5.58±0.83% and 13.6±4.60%, respectively. Based on our previous work [155], the change of LER value is directly affected by the grain size. Since the Ar atmosphere accelerates grain growth in comparison to the air atmosphere, the ZnO ridges sintered in Ar show higher LER values, demonstrating that faster grain growth leads to more feature fidelity loss. At longer

sintering time of 480 min, the discontinuity of the ZnO ridges increases the LER value dramatically.
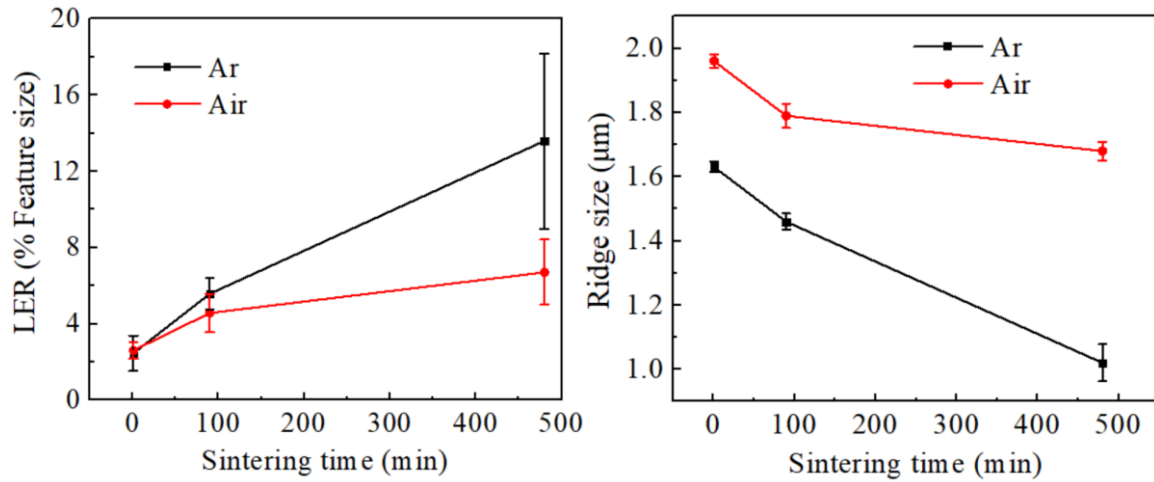
Fig. 4.3. (a) LER values of the sintered ZnO ridges in different atmospheres and (b) average ridge sizes of the sintered ZnO ridges in different atmospheres.

Fig. 4.3b shows the ridge sizes of the ZnO samples sintered in air and argon atmospheres at 1000°C. When the sintering time is 1, 90, and 480 min, the ZnO ridge size in argon is 1.63±0.02, 1.46±0.03 and 1.02±0.06 μm, respectively, and the ridge size of the ZnO features sintered in air is 1.96±0.02, 1.79±0.04 and 1.68±0.03 μm, respectively. The ridge width for the samples sintered in the Ar atmosphere is always smaller than that sintered in the air atmosphere at the same sintering time. With the sintering time increase, the Ar-sintered ridge features show smaller width than that of the air-sintered ridges.

Another important observation is that the ZnO bulk and features shrink differently (Fig. 4.4). As an example, after the 480 min sintering in argon and air atmospheres, the linear shrinkage values of the features are 47.42% and 25.53%, respectively; whereas, the linear shrinkage values of the bulks are 23.62% and 22.40%, respectively. As ZnO material has the intrinsic decomposition and evaporation effect during sintering [153], it is another reason for the so large apparent linear shrinkage value of 47.42%. Therefore, the combination of the densification and the evaporation contribute the final reduction of the sintered ridge width.
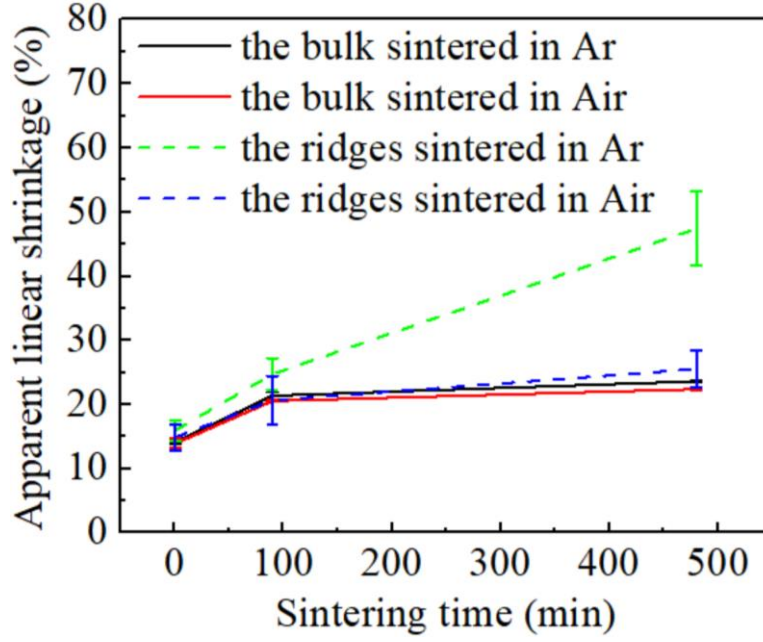
Fig. 4.4. Apparent linear shrinkages of the bulks and features sintered in air and Ar.

4.3.3 Evaporation and densification analysis of ZnO ridges

For the reduction of ridge size, two processes work simultaneously: the densification process resulting from sintering and decomposition process resulting from decomposition. The effect of the decomposition process can be estimated by comparing linear shrinkage values of the features and bulks. For the 8 hrs sintering in argon and air atmospheres, the linear shrinkage values of the features are 37.42% and 14. 29%, respectively; the linear shrinkage values of the bulks are 11.07% and 9.82%, respectively. Increasing of the linear shrinkage values results from the mass loss due to the decomposition. The sintering atmosphere will affect the decomposition rate of ZnO during sintering. For the decomposition of ZnO, based on equations (4.1) and (4.2), the reaction rate v_P can be expressed as:

$$v_P \propto P_{O_2}{}^d \tag{4.10}$$

where, P_{O_2} is the concentration of the oxygen, d is the reaction order. Based on equations (4.10), the net reaction rate in a specific surface area can be estimated by:

$$v = k_1[O_2]^b \tag{4.11}$$

where dm is the mass change in dt and k_1 is the reaction rate constant. In argon and air atmospheres, the increase of decomposition rate will be reflected in the linear shrinkage value of the features. The linear shrinkage resulting from the decomposition is defined as extra shrinkage S_e. The value of S_e can be obtained by calculating the difference between the actual linear shrinkage and the linear shrinkage resulting from densification. Since the grain size is much smaller than the ridge size, the linear shrinkage from densification can be estimated by

51

the linear shrinkage of the bulk. The relationship between extra linear shrinkage from the decomposition process and oxygen partial pressure can be expressed as:

$$S_e = k_1[O_2]^b \tag{4.12}$$

Based on the experimental result in fig. 4.3b, the value of b is ~-0.14 and the value of k_1 is ~-0.0088. For air atmosphere, the redeposition rate is relatively high, the effect of the decomposition on sintering behaviors are not obvious. For argon atmosphere, the partial pressure is much lower than that of air atmospheres. The effect of the decomposition on the feature size is much more obvious.

4.3.4   3D reconstruction of sintered ZnO ridges

The densification rate difference resulting from scale and atmosphere is demonstrated by 3D reconstruction techniques. Fig. 4.5a and 4.5b show the cross-sections of the sintered ZnO ridges in air and Ar, respectively. It is obvious that grains grow much faster in Ar atmosphere compared to air atmosphere. Based on the series (30 slices) of the cross-section images, the microstructures of the ridges are reconstructed and the corresponding relative densities are obtained. The relative densities of the ridges sintered in air and Ar are 91.3% and 93.2%, respectively. It is proved that the ridges have higher densification rates than the bulks and Ar atmosphere can accelerate the densification rate in comparison to air atmosphere.
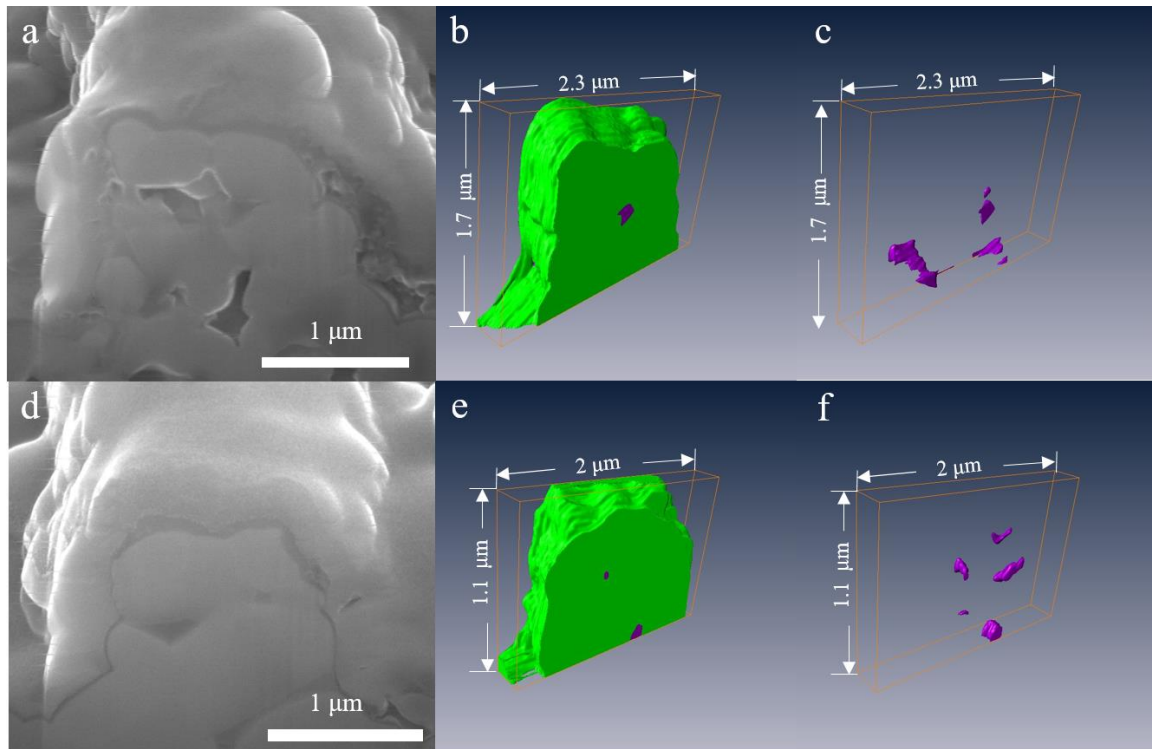
Fig. 4.5. Slice view of the ridges sintered in air (a) and Ar (d); 3D reconstruction and the corresponding pore structure images of a part of the ridges sintered in air (b, c) and Ar (e, f).

4.4 Conclusions

Micron-sized ZnO ridges were sintered in air and argon atmosphere. Obvious differences are found in densification rate and size change of the ZnO ridges. Argon atmosphere accelerates the densification rate by increasing the vacancy concentration on the grain surface. Besides, in the argon atmosphere, the enhanced decomposition of ZnO will cause extra reduction of the ZnO ridge size. The effect of oxygen particle pressure on densification and size reduction of the ZnO feature is analyzed quantitatively. The evaporation effect and Zn interstitial are combined to lead the sintering difference in air and argon.

5 Conclusions

In this thesis, micron- and submicron-sized ceramic patterns (from 2 μm to 400 nm) with high fidelity are fabricated via centrifuge-aided micromolding. For 2 μm ridges, when 7000 rpm condition is used, the introduction of centrifugal force increases the patterning rate by ~ 20000 times and reduces the linear shrinkage by ~ 4% during the drying process. Ideal models are established to explain the patterning process, and quantitative relationships between the feature size, patterning time, and centrifugal condition are established. Sintering behaviors of the ceramic features are different from that of ceramic bulks, including faster densification and slower grain growth. Feature destruction and surface roughness occur due to the abnormal grain growth. With a sintering process at 950 °C with 8 hrs holding time, the LER value of 2 μm ridges increases from 2% to 10% and the circularity of 2 μm rods decreases from 0.90 to 0.64. Feature destruction time can be predicted based on grain growth. For 2 μm ridge, the destruction time at 950 °C is about 4.1 hrs. Surface roughening process is further explained based on the chemical potential difference between grain surface and grain boundary. Sintering atmosphere has a significant influence on the morphological evolution and densification rate of micron-sized ZnO ridges due to evaporation tendency. Oxygen particle pressure affects densification rate of the ZnO bulk and size reduction of the ZnO feature. Low oxygen content in the sintering atmosphere will result in a faster densification rate and more mass loss. Fundamental theories and mathematical expressions are established to explain and predict the difference in densification rate of the bulks and size reduction of the features.

Publications

1. **H.-F. Ju**, K. Ning, and K. Lu, "Sintering behaviors of micron-sized ceramic rod features," *Acta Materialia*, 144: 534-542 (2018).

2. **H.-F. Ju**, K. Ning, and K. Lu, "Roughening and destructive effects of sintering on micron-sized ZnO features," *Acta Materialia*, 141: 352-359 (2017).

3. **H.-F. Ju**, K. Ning, and K. Lu, "Centrifuge-aided micromolding of micron-and submicron-sized patterns," *Journal of the European Ceramic Society*, 38[2]: 637-645 (2018).

4. K. Ning, **H.-F. Ju**, K. Bawane, and K. Lu, "Spark plasma sintering of silicon carbide-nanostructured ferritic alloy composites with chromium carbide barrier layer," *Materials Science and Engineering: A*, 700[17]: 183-190 (2017).

References

1. Y. Xia and G. M. Whitesides, "Soft lithography," *Annual Review of Materials Science,* 28[1] 153-84 (1998).

2. J. A. Rogers, K. E. Paul, R. J. Jackman, and G. M. Whitesides, "Using an elastomeric phase mask for sub-100 nm photolithography in the optical near field," *Applied Physics Letters,* 70[20] 2658-60 (1997).

3. S. Reyntjens and R. Puers, "A review of focused ion beam applications in microsystem technology," *Journal of Micromechanics and Microengineering,* 11[4] 287-300 (2001).

4. S. Jeon, E. Menard, J. U. Park, J. Maria, M. Meitl, J. Zaumseil, and J. A. Rogers, "Three-dimensional nanofabrication with rubber stamps and conformable photomasks," *Advanced Material,* 16[15] 1369-73 (2004).

5. A. A. Tseng, K. Chen, C. D. Chen, and K. J. Ma, "Electron beam lithography in nanoscale fabrication: recent development," *IEEE Transactions on Electronics Packaging Manufacturing,* 26[2] 141-49 (2003).

6. Y. N. Xia and G. M. Whitesides, "Soft lithography," *Angewandte Chemie International Edition,* 37[5] 550-75 (1998).

7. Y. N. Xia, J. J. McClelland, R. Gupta, D. Qin, X. M. Zhao, L. L. Sohn, R. J. Celotta, and G. M. Whitesides, "Replica molding using polymeric materials: A practical step toward nanomanufacturing," *Advanced Material,* 9[2] 147-49 (1997).

8. C. Yang, C.-H. Choi, C.-S. Lee, and H. Yi, "A facile synthesis–fabrication strategy for integration of catalytically active viral-palladium nanostructures into polymeric hydrogel microparticles via replica molding," *ACS Nano,* 7[6] 5032-44 (2013).

9. W. R. Childs and R. G. Nuzzo, "Decal transfer microlithography: A new soft-lithographic patterning method," *Journal of the American Chemical Society,* 124[45] 13583-96 (2002).

10. X. M. Zhao, Y. N. Xia, and G. M. Whitesides, "Fabrication of three-dimensional micro-structures: Microtransfer molding," *Advanced Material,* 8[10] 837-40 (1996).

11. N. Naik, J. Caves, E. L. Chaikof, and M. G. Allen, "Generation of spatially aligned collagen fiber networks through microtransfer molding," *Advanced Healthcare Materials,* 3[3] 367-74 (2014).

12. E. Kim, Y. N. Xia, and G. M. Whitesides, "Polymer microstructures formed by molding in capillaries," *Nature,* 376[6541] 581-84 (1995).

13. Q. B. Xu, R. M. Rioux, M. D. Dickey, and G. M. Whitesides, "Nanoskiving: A new method to produce arrays of nanostructures," *Accounts of Chemical Research,* 41[12] 1566-77 (2008).

14. E. Kim, Y. N. Xia, X. M. Zhao, and G. M. Whitesides, "Solvent-assisted microcontact molding: A convenient method for fabricating three-dimensional structures on surfaces of polymers," *Advanced Materials,* 9[8] 651-54 (1997).

15. S. A. Veldhuis, A. George, M. Nijland, and J. E. ten Elshof, "Concentration dependence on the shape and size of sol–gel-derived yttria-stabilized zirconia ceramic features by soft lithographic patterning," *Langmuir,* 28[42] 15111-17 (2012).

16. B. Su, J. Meng, and Z. Zhang, "Crack-free drying of ceramic microparts on a hydrophobic flexible polymer substrate using soft lithography," *Journal of the American Chemical Society,* 99[4] 1141-43 (2016).

17. S. Y. Chou, P. R. Krauss, W. Zhang, L. Guo, and L. Zhuang, "Sub-10 nm imprint lithography and applications," *Journal of Vacuum Science & Technology B,* 15[6] 2897-904 (1997).

18. H. Kim, M.-W. Jung, S. Myung, D. Jung, S. S. Lee, K.-J. Kong, J. Lim, J.-H. Lee, C. Y. Park, and K.-S. An, "Soft lithography of graphene sheets via surface energy modification," *Journal of Material Chemistry C,* 1[6] 1076-79 (2013).

19. M. G. Kim, H. Alrowais, S. Pavlidis, and O. Brand, "Size-scalable and high-density liquid-metal-based soft electronic passive components and circuits using soft lithography," *Advanced Functional Material,* 27[3] 16044-66 (2016).

20. J. Coulm, D. Léonard, C. Desroches, and F. Bessueille, "Formation and use of palladium (II)–thiol complexes at the surface of PDMS stamps for the fabrication of high resolution and high density metal patterns using soft-lithography techniques," *Colloids and Surfaces A: Physicochemical and Engineering Aspects,* 466[5] 75-84 (2015).

21. Y. N. Xia, J. A. Rogers, K. E. Paul, and G. M. Whitesides, "Unconventional methods for fabricating and patterning nanostructures," *Chemical Review,* 99[7] 1823-48 (1999).

22. Z. W. Li, Y. N. Gu, L. Wang, H. X. Ge, W. Wu, Q. F. Xia, C. S. Yuan, Y. Chen, B. Cui, and R. S. Williams, "Hybrid nanoimprint-soft lithography with sub-15 nm resolution," *Nano Letter,* 9[6] 2306-10 (2009).

23. Y. N. Xia and G. M. Whitesides, "Soft lithography," *Annual Review of Materials Research,* 28[1] 153-84 (1998).

24. D. Qin, Y. N. Xia, and G. M. Whitesides, "Soft lithography for micro- and nanoscale patterning," *Nature Protocols,* 5[3] 491-502 (2010).

25. H. D. Kim, T. Nakayama, B. J. Hong, K. Imaki, T. Yoshimura, T. Suzuki, H. Suematsu, and K. Niihara, "Fine-structured ZnO patterns with sub-micrometer on the ceramic surface fabricated by a replication method," *Journal of the Ceramic Society of Japan,* 118[1384] 1140-43 (2010).

26. M. J. Hampton, S. S. Williams, Z. Zhou, J. Nunes, D. H. Ko, J. L. Templeton, E. T. Samulski, and J. M. DeSimone, "The patterning of sub-500 nm inorganic oxide structures," *Advanced Materials,* 20[14] 2667-73 (2008).

27. A. Mukherjee, B. Maiti, A. Das Sharma, R. N. Basu, and H. S. Maiti, "Correlation between slurry rheology, green density and sintered density of tape cast yttria stabilised zirconia," *Ceramic International,* 27[7] 731-39 (2001).

28. R. Greenwood and K. Kendall, "Selection of suitable dispersants for aqueous suspensions of zirconia and titania powders using acoustophoresis," *Journal of the European Ceramic Society,* 19[4] 479-88 (1999).

29. J. J. Guo and J. A. Lewis, "Aggregation effects on the compressive flow properties and drying behavior of colloidal silica suspensions," *Journal of the American Ceramic Society,* 82[9] 2345-58 (1999).

30. F. F. Lange, "Powder processing science and technology for increased reliability," *Journal of the American Ceramic Society,* 72[1] 3-15 (1989).

31. K. T. Miller, R. M. Melant, and C. F. Zukoski, "Comparison of the compressive yield response of aggregated suspensions: Pressure filtration, centrifugation, and osmotic consolidation," *Journal of the American Ceramic Society,* 79[10] 2545-56 (1996).

32. R. Buscall, "The sedimentation of concentrated colloidal suspensions," *Colloids and Surfaces,* 43[1] 33-53 (1990).

33. W. H. Shih, W. Y. Shih, S. I. Kim, and I. A. Aksay, "Equilibrium-state density profiles of centrifuged cakes," *Journal of the American Ceramic Society,* 77[2] 540-46 (1994).

34. M. Rahaman and M. N. Rahaman, "Ceramic processing.*"* CRC press, (2006).

35. C. Tian and S. W. Chan, "Ionic conductivities, sintering temperatures and microstructures of bulk ceramic CeO_2 doped with Y_2O_3," Solid State Ionics, 134[1]: 89-102 (2000).

36. A. Polotai, K. Breece, E. Dickey, C. Randall, and A. Ragulya, "A novel approach to sintering nanocrystalline barium titanate ceramics," *Journal of the American Ceramic Society,* 88[11] 3008-12 (2005).

37. K. Araki and J. W. Halloran, "Porous ceramic bodies with interconnected pore channels by a novel freeze casting technique," *Journal of the American Ceramic Society,* 88[5] 1108-14 (2005).

38. M. Matsubara, T. Yamaguchi, K. Kikuta, and S.-i. Hirano, "Sinterability and piezoelectric properties of (K, Na)NbO$_3$ ceramics with novel sintering aid," *Japanese Journal of Applied Physics,* 43[10] 7159-63 (2004).

39. Q. Liu, K. A. Khor, S. Chan, and X. Chen, "Anode-supported solid oxide fuel cell with yttria-stabilized zirconia/gadolinia-doped ceria bilalyer electrolyte prepared by wet ceramic co-sintering process," *Journal of Power Sources,* 162[2] 1036-42 (2006).

40. G.-H. Chen and X.-Y. Liu, "Sintering, crystallization and properties of MgO–Al$_2$O$_3$–SiO$_2$ system glass-ceramics containing ZnO," *Journal of Alloys and Compounds,* 431[1] 282-86 (2007).

41. K. Agrawal, G. Singh, D. Puri, and S. Prakash, "Synthesis and characterization of hydroxyapatite powder by sol-gel method for biomedical application," *Journal of Minerals and Materials Characterization and Engineering,* 10[8] 727-734 (2011).

42. K. Chu, H. Guo, C. Jia, F. Yin, X. Zhang, X. Liang, and H. Chen, "Thermal properties of carbon nanotube–copper composites for thermal management applications," *Nanoscale research letters,* 5[5] 868-874 (2010).

43. R. S. Mishra, C. E. Lesher, and A. K. Mukherjee, "High-pressure sintering of nanocrystalline γ-Al$_2$O$_3$," *Journal of the American Ceramic Society,* 79[11] 2989-92 (1996).

44. I.-W. Chen and X.-H. Wang, "Sintering dense nanocrystalline ceramics without final-stage grain growth," *Nature,* 404[6774] 168-71 (2000).

45. D. K. Agrawal, "Microwave processing of ceramics," *Current Opinion in Solid State and Materials Science,* 3[5] 480-85 (1998).

46. M. Cologna, B. Rashkova, and R. Raj, "Flash sintering of nanograin zirconia in< 5 s at 850 C," *Journal of the American Ceramic Society,* 93[11] 3556-59 (2010).

47. C. Legros, C. Carry, P. Bowen, and H. Hofmann, "Sintering of a transition alumina: effects of phase transformation, powder characteristics and thermal cycle," *Journal of the European Ceramic Society,* 19[11] 1967-78 (1999).

48. J. Tong, D. Clark, M. Hoban, and R. O'Hayre, "Cost-effective solid-state reactive sintering method for high conductivity proton conducting yttrium-doped barium zirconium ceramics," *Solid State Ionics,* 181[11] 496-503 (2010).

49. Z. Munir, U. Anselmi-Tamburini, and M. Ohyanagi, "The effect of electric field and pressure on the synthesis and consolidation of materials: a review of the spark plasma sintering method," *Journal of Materials Science,* 41[3] 763-77 (2006).

50. J. G. Li and X. D. Sun, "Synthesis and sintering behavior of a nanocrystalline alpha-alumina powder," *Acta Materialia,* 48[12] 3103-12 (2000).

51. D. M. Zhu and R. A. Miller, "Sintering and creep behavior of plasma-sprayed zirconia- and hafnia-based thermal barrier coatings," *Surface and Coatings Technology,* 108[1-3] 114-20 (1998).

52. A. C. F. Cocks, "The structure of constitutive laws for the sintering of fine-grained materials," *Acta Metallurgica et Materialia,* 42[7] 2191-210 (1994).

53. P. Duran, J. Tartaj, J. F. Fernandez, M. Villegas, and C. Moure, "Crystallisation and sintering behaviour of nanocrystalline Y-TZP powders obtained by seeding-assisted chemical coprecipitation," *Ceramics International,* 25[2] 125-35 (1999).

54. G. S. A. M. Theunissen, A. J. A. Winnubst, and A. J. Burggraaf, "Sintering kinetics and microstructure development of nanoscale Y-Tzp ceramics," *Journal of the European Ceramic Society,* 11[4] 315-24 (1993).

55. R. K. Bordia, S. J. L. Kang, and E. A. Olevsky, "Current understanding and future research directions at the onset of the next century of sintering science and technology," *Journal of the American Ceramic Society,* 100[6] 2315-52 (2017).

56. S.-J. L. Kang, "Sintering: densification, grain growth and microstructure." Butterworth-Heinemann, (2004).

57. A. L. Maximenko and E. A. Olevsky, "Effective diffusion coefficients in solid-state sintering," *Acta Materialia,* 52[10] 2953-63 (2004).

58. S.-J. L. Kang and Y.-I. Jung, "Sintering kinetics at final stage sintering: model calculation and map construction," *Acta Materialia,* 52[15] 4573-78 (2004).

59. G. Bernard-Granger and C. Guizard, "New relationships between relative density and grain size during solid-state sintering of ceramic powders," *Acta Materialia,* 56[20] 6273-82 (2008).

60. R. M. German, "Coarsening in sintering: grain shape distribution, grain size distribution, and grain growth kinetics in solid-pore systems," *Critical reviews in solid state and materials sciences,* 35[4] 263-305 (2010).

61. I. W. Chen and X. H. Wang, "Sintering dense nanocrystalline ceramics without final-stage grain growth," *Nature,* 404[6774] 168-71 (2000).

62. C. P. Cameron and R. Raj, "Grain-growth transition during sintering of colloidally prepared alumina powder compacts," *Journal of the American Ceramic Society,* 71[12] 1031-35 (1988).

63. Z. Liu, J. S. Cronin, K. Yu-chen, J. R. Wilson, K. J. Yakal-Kremski, J. Wang, K. T. Faber, and S. A. Barnett, "Three-dimensional morphological measurements of $LiCoO_2$ and $LiCoO_2$/Li $(Ni_{1/3}Mn_{1/3}Co_{1/3})O_2$ lithium-ion battery cathodes," *Journal of Power Sources,* 227[1] 267-74 (2013).

64. X. Guo and J. Maier, "Grain boundary blocking effect in zirconia: A Schottky barrier analysis," *Journal of The Electrochemical Society,* 148[3] 121-26 (2001).

65. T. Kosmac, C. Oblak, P. Jevnikar, N. Funduk, and L. Marion, "Strength and reliability of surface treated Y-TZP dental ceramics," *Journal of Biomedical Materials Research,* 53[4] 304-13 (2000).

66. Z. Fang and H. Wang, "Densification and grain growth during sintering of nanosized particles," *International Materials Reviews,* 53[6] 326-52 (2008).

67. F. Wakai, M. Yoshida, and B. P. Kashyap, "Influence of particle arrangement on coarsening during sintering of three spherical particles," *Journal of the Ceramic Society of Japan,* 114[1335] 974-78 (2006).

68. H. Wang, Z. Z. Fang, and K. S. Hwang, "Kinetics of initial coarsening during sintering of nanosized powders," *Metallurgical and Materials Transactions A,* 42[11] 3534-42 (2011).

69. J. Fang, A. M. Thompson, M. P. Harmer, and H. M. Chan, "Effect of yttrium and lanthanum on the final-stage sintering behavior of ultrahigh-purity alumina," *Journal of the American Ceramic Society,* 80[8] 2005-12 (1997).

70. P. L. Chen and I. W. Chen, "Sintering of fine oxide powders: II, sintering mechanisms," *Journal of the American Ceramic Society,* 80[3] 637-45 (1997).

71. H. Lee and R. F. Speyer, "Pressureless sintering of boron carbide," *Journal of the American Ceramic Society,* 86[9] 1468-73 (2003).

72. C. R. Martin and I. A. Aksay, "Topographical evolution of lead zirconate titanate (PZT) thin films patterned by micromolding in capillaries," *The Journal of Physical Chemistry B,* 107[18] 4261-68 (2003).

73. T. Rosqvist and S. Johansson, "Soft micromolding and lamination of piezoceramic thick films," *Sensors and Actuators A: Physical,* 97[1] 512-19 (2002).

74. A. Bertsch, S. Jiguet, and P. Renaud, "Microfabrication of ceramic components by microstereolithography," *Journal of Micromechanics and Microengineering,* 14[2] 197-203 (2004).

75. M. Nygren and Z. J. Shen, "On the preparation of bio-, nano- and structural ceramics and composites by spark plasma sintering," *Solid State Science,* 5[1] 125-31 (2003).

76. L. An, H. Chan, and K. Soni, "Control of calcium hexaluminate grain morphology in in-situ toughened ceramic composites," *Journal of Materials Science,* 31[12] 3223-29 (1996).

77. M. Heule and L. J. Gauckler, "Gas sensors fabricated from ceramic suspensions by micromolding in capillaries," *Advanced Materials,* 13[23] 1790-93 (2001).

78. H. Yang, P. Deschatelets, S. T. Brittain, and G. M. Whitesides, "Fabrication of high performance ceramic microstructures from a polymeric precursor using soft lithography," *Advanced Materials,* 13[1] 54-58 (2001).

79. U. P. Schönholzer and L. J. Gauckler, "Ceramic parts patterned in the micrometer range," *Advanced Materials,* 11[8] 630-32 (1999).

80. W. D. Kingery and M. Berg, "Study of the initial stages of sintering solids by viscous flow, evaporation-condensation, and self-diffusion," *Journal of Applied Physics,* 26[10] 1205-12 (1955).

81. U. Ozgur, D. Hofstetter, and H. Morkoc, "ZnO devices and applications: A review of current status and future prospects," *Proceedings of the IEEE,* 98[7] 1255-68 (2010).

82. U. Ozgur, Y. I. Alivov, C. Liu, A. Teke, M. A. Reshchikov, S. Dogan, V. Avrutin, S. J. Cho, and H. Morkoc, "A comprehensive review of ZnO materials and devices," *Journal of Applied Physics,* 98[4] 1-104 (2005).

83. A. P. Hynes, R. H. Doremus, and R. W. Siegel, "Sintering and characterization of nanophase zinc oxide," *Journal of the American Ceramic Society,* 85[8] 1979-87 (2002).

84. T. Gray, "Sintering of zinc oxide," *Journal of the American Ceramic Society,* 37[11] 534-38 (1954).

85. K. G. Ewsuk, D. T. Ellerby, and C. B. DiAntonio, "Analysis of nanocrystalline and microcrystalline ZnO sintering using master sintering curves," *Journal of the American Ceramic Society,* 89[6] 2003-09 (2006).

86. L. Gao, Q. Li, W. Luan, H. Kawaoka, T. Sekino, and K. Niihara, "Preparation and electric properties of dense nanocrystalline zinc oxide ceramics," *Journal of the American Ceramic Society,* 85[4] 1016-18 (2002).

87. B. Ye, E.-S. Kim, M. Cui, J. Khim, J. M. Baik, and H.-D. Kim, "Fine-structured oxide ceramics from a novel replication method," *Ceramics International,* 42[9] 10872-78 (2016).

88. X. M. Zhao, Y. N. Xia, and G. M. Whitesides, "Fabrication of three-dimensional micro-structures: Microtransfer molding," *Advanced Materials,* 8[10] 837-840 (1996).

89. E. Kim, Y. Xia, and G. M. Whitesides, "Polymer microstructures formed by molding in capillaries," *Nature,* 376[6541] 581-84 (1995).

90. R. Schirhagl, U. Latif, D. Podlipna, H. Blumenstock, and F. L. Dickert, "Natural and biomimetic materials for the detection of insulin," *Analytical chemistry,* 84[9] 3908-13 (2012).

91. M. g. Kim, H. Alrowais, S. Pavlidis, and O. Brand, "Size-scalable and high-density liquid-metal-based soft electronic passive components and circuits using soft lithography," *Advanced Functional Materials,* 27[3] 1-11 (2016).

92. B. Su, J. Meng, and Z. Zhang, "Crack-free drying of ceramic microparts on a hydrophobic flexible polymer substrate using soft lithography," *Journal of the American Ceramic Society,* 99[4] 1141-1143 (2016).

93. J. A. Lewis, "Colloidal processing of ceramics," *Journal of the American Ceramic Society,* 83[10] 2341-59 (2000).

94. B. Chen, K. Lu, and K. Ramsburg, "ZnO submicrometer rod array by soft lithographic micromolding with high solid loading nanoparticle suspension," *Journal of the American Ceramic Society,* 96[1] 73-79 (2013).

95. S.-D. Kim, H. Wada, and J. C. Woo, "TCAD-based statistical analysis and modeling of gate line-edge roughness effect on nanoscale MOS transistor performance and scaling," *IEEE transactions on Semiconductor Manufacturing,* 17[2] 192-200 (2004).

96. K. Lu, C. S. Kessler, and R. M. Davis, "Optimization of a nanoparticle suspension for freeze casting," *Journal of the American Ceramic Society,* 89[8] 2459-65 (2006).

97. K. Lu and C. Kessler, "Colloidal dispersion and rheology study of nanoparticles," *Journal of materials science,* 41[17] 5613-18 (2006).

98. K. Lu and C. Hammond, "Nanoparticle-based surface templating," *The International Journal of Applied Ceramic Technology,* 8[4] 965-76 (2011).

99. K. Lu, "Rheological behavior of carbon nanotube-alumina nanoparticle dispersion systems," *Powder Technology,* 177[3] 154-61 (2007).

100. D. Zhang, B. Su, and T. W. Button, "Improvements in the structural integrity of green ceramic microcomponents by a modified soft moulding process," *Journal of the European Ceramic Society,* 27[2-3] 645-50 (2007).

101. Y. H. Gong, C. Shen, Y. Z. Lu, H. Meng, and C. X. Li, "Viscosity and density measurements for six binary mixtures of water (methanol or ethanol) with an ionic liquid ([BMIM][DMP] or [EMIM][DMP]) at atmospheric pressure in the temperature range of (293.15 to 333.15) K," *Journal of Chemical & Engineering Data,* 57[1] 33-39 (2012).

102. D. R. Lide, "CRC handbook of chemistry and physics " *Boca Raton (FL): CRC Press* (2005).

103. X. H. Yang and W. L. Zhu, "Viscosity properties of sodium carboxymethylcellulose solutions," *Cellulose,* 14[5] 409-17 (2007).

104. A. Asenov, S. Kaya, and A. R. Brown, "Intrinsic parameter fluctuations in decananometer MOSFETs introduced by gate line edge roughness," *IEEE Transactions on Electron Devices,* 50[5] 1254-60 (2003).

105. K. Seong-Dong, H. Wada, and J. C. S. Woo, "TCAD-based statistical analysis and modeling of gate line-edge roughness effect on nanoscale MOS transistor performance and scaling," *IEEE Transactions on Semiconductor Manufacturing,* 17[2] 192-200 (2004).

106. A. Yamaguchi, H. Fukuda, T. Arai, J. Yamamoto, T. Hirayama, D. Shiono, H. Hada, and J. Onodera, "Spectral analysis of line-edge roughness in polyphenol EB-resists and its impact on transistor performance," *Journal of Vacuum Science & Technology B,* 23[6] 2711-15 (2005).

107. D. Myers, "Surfaces, interfaces and colloids.*"* Wiley-Vch New York etc., (1990).

108. I. A. AKSAY, "Consolidation of colloidal suspensions," *Better Ceramics Through Chemistry,* 23[15]167-172 (1990).

109. I. D. Johnston, D. K. McCluskey, C. K. L. Tan, and M. C. Tracey, "Mechanical characterization of bulk Sylgard 184 for microfluidics and microengineering," *Journal of Micromechanics and Microengineering,* 24[3] 1-7 (2014).

110. I. Johnston, D. McCluskey, C. Tan, and M. Tracey, "Mechanical characterization of bulk Sylgard 184 for microfluidics and microengineering," *Journal of Micromechanics and Microengineering,* 24[3] 1-7 (2014).

111. K. Lu, "Freeze cast carbon nanotube-alumina nanoparticle green composites," *Journal of Materials Science,* 43[2] 652-59 (2008).

112. K. Lu and X. J. Zhu, "Freeze casting as a nanoparticle material-forming method," *International Journal of Applied Ceramic Technology,* 5[3] 219-27 (2008).

113. D. H. Sharp, "An overview of Rayleigh-Taylor instability," *Physica D: Nonlinear Phenomena,* 12[1] 3-18 (1984).

114. M. Ishii and T. Hibiki, "Thermo-fluid dynamics of two-phase flow.*"* Springer Science & Business Media, (2010).

115. G. W. Scherer, "Theory of drying," *Journal of the American Ceramic Society,* 73[1] 3-14 (1990).

116. M. L. Gonzalez-Martin, L. Labajos-Broncano, B. Janczuk, and J. M. Bruque, "Wettability and surface free energy of zirconia ceramics and their constituents," *Journal of Materials Science,* 34[23] 5923-26 (1999).

117. G. Y. Onoda, "Theoretical strength of dried green bodies with organic binders," *Journal of the American Ceramic Society,* 59[5-6] 236-39 (1976).

118. J. Voldman, M. L. Gray, and M. A. Schmidt, "Microfabrication in biology and medicine," *Annual Review of Biomedical Engineering,* 1[1] 401-25 (1999).

119. J.-Z. Li, T. Wu, Z.-Y. Yu, L. Zhang, G.-Q. Chen, and D.-M. Guo, "Micro machining of pre-sintered ceramic green body," *Journal of Materials Processing Technology,* 212[3] 571-79 (2012).

120. G. M. Whitesides, "The origins and the future of microfluidics," *Nature,* 442[7101] 368-73 (2006).

121. L. J. Guo, "Nanoimprint lithography: methods and material requirements," *Advanced Material,* 19[4] 495-513 (2007).

122. P. Kim, K. W. Kwon, M. C. Park, S. H. Lee, S. M. Kim, and K. Y. Suh, "Soft lithography for microfluidics: A review," *BioChip Journal,* 2[1] 1-11 (2008).

123. O. F. Gobel, M. Nedelcu, and U. Steiner, "Soft lithography of ceramic patterns," *Advanced Functional Material,* 17[7] 1131-36 (2007).

124. K. H. Park, I. K. Sung, and D. P. Kim, "Fabrication of SiC-based ceramic patterns via soft lithography of polymeric precursors," *Key Engineering Material,* 287[1330] 96-101 (2005).

125. Y. Zhang and J. Luo, "Promoting the flash sintering of ZnO in reduced atmospheres to achieve nearly full densities at furnace temperatures of< 120 C," *Scripta Materialia,* 106[1] 26-29 (2015).

126. G. L. Messing, S. Trolier-McKinstry, E. Sabolsky, C. Duran, S. Kwon, B. Brahmaroutu, P. Park, H. Yilmaz, P. Rehrig, and K. Eitel, "Templated grain growth of textured piezoelectric ceramics," *Critical Reviews in Solid State and Materials Sciences,* 29[2] 45-96 (2004).

127. O.-S. Kwon, S.-H. Hong, J.-H. Lee, U.-J. Chung, D.-Y. Kim, and N. Hwang, "Microstructural evolution during sintering of TiO_2/SiO_2-doped alumina: mechanism of anisotropic abnormal grain growth," *Acta Materialia,* 50[19] 4865-72 (2002).

128. U. Ozgur, Y. I. Alivov, C. Liu, A. Teke, M. A. Reshchikov, S. Dogan, V. Avrutin, S. J. Cho, and H. Morkoc, "A comprehensive review of ZnO materials and devices," *Journal of Applied Physics,* 98[4]1-103 (2005).

129. H.-F. Ju, K. Ning, and K. Lu, "Centrifuge-aided micromolding of micron-and submicron-sized patterns," *Journal of the European Ceramic Society*, 38[2]: 637-645 (2018).

130. C. Tang, M. J. Spencer, and A. S. Barnard, "Activity of ZnO polar surfaces: an insight from surface energies," *Physical Chemistry Chemical Physics,* 16[40] 39-44 (2014).

131. F. Ernst, O. Kienzle, and M. Rühle, "Structure and composition of grain boundaries in ceramics," *Journal of the European Ceramic Society,* 19[6] 665-73 (1999).

132. W. Jo, D. Y. Kim, and N. M. Hwang, "Effect of interface structure on the microstructural evolution of ceramics," *Journal of the American Ceramic Society,* 89[8] 2369-80 (2006).

133. B.-K. Lee, S.-Y. Chung, and S.-J. L. Kang, "Grain boundary faceting and abnormal grain growth in $BaTiO_3$," *Acta Materialia,* 48[7] 1575-80 (2000).

134. P. Ruterana, M. Abouzaid, A. Bere, and J. Chen, "Formation of a low energy grain boundary in ZnO: The structural unit concept in hexagonal symmetry materials," *Journal of Applied Physics,* 103[3] 033501-1-7 (2008).

135. H. Morkoç and Ü. Özgür, "Zinc oxide." in. Wiley-VCH Verlag GmbH & Co. KGaA, 2007.

136. M. J. Mayo, "Processing of nanocrystalline ceramics from ultrafine particles," *International Materials Reviews,* 41[3] 85-115 (1996).

137. K. Bodišová, D. Galusek, P. Švančárek, V. Pouchlý, and K. Maca, "Grain growth suppression in alumina via doping and two-step sintering," *Ceramics International,* 41[9] 11975-83 (2015).

138. H. Inaba, T. Nakajima, and H. Tagawa, "Sintering behaviors of ceria and gadolinia-doped ceria," *Solid State Ionics,* 106[3] 263-68 (1998).

139. N. Canikoğlu, N. Toplan, K. Yıldız, and H. Ö. Toplan, "Densification and grain growth of SiO2-doped ZnO," *Ceramics International,* 32[2] 127-32 (2006).

140. E. Kim, Y. Xia, and G. M. Whitesides, "Polymer microstructures formed by moulding in capillaries," *Nature,* 376[6541] 581-584 (1995).

141. M. C. Gather, A. Koehnen, A. Falcou, H. Becker, and K. Meerholz, "Solution-processed full-color polymer organic light-emitting diode displays fabricated by direct photolithography," *Advanced Functional Materials,* 17[2] 191-200 (2007).

142. Z. Zhu, X. Wei, and K. Jiang, "A net-shape fabrication process of alumina micro-components using a soft lithography technique," *Journal of Micromechanics and Microengineering,* 17[2] 193-198 (2006).

143. S. C. Pillai, J. M. Kelly, D. E. McCormack, P. O'Brien, and R. Ramesh, "The effect of processing conditions on varistors prepared from nanocrystalline ZnO," *Journal of Materials Chemistry,* 13[10] 86-90 (2003).

144. Q. Wan, Q. Li, Y. Chen, T.-H. Wang, X. He, J. Li, and C. Lin, "Fabrication and ethanol sensing characteristics of ZnO nanowire gas sensors," *Applied Physics Letters,* 84[18] 3654-56 (2004).

145. H. Liu, V. Avrutin, N. Izyumskaya, Ü. Özgür, and H. Morkoç, "Transparent conducting oxides for electrode applications in light emitting and absorbing devices," *Superlattices and Microstructures,* 48[5] 458-84 (2010).

146. Z. L. Wang, "Zinc oxide nanostructures: growth, properties and applications," *Journal of Physics: Condensed Matter,* 16[25] R829 (2004).

147. J. Roberts and C. Wheeler, "Diffusion of zinc in polycrystalline zinc oxide," *Transactions of the Faraday Society,* 56[] 570-80 (1960).

148. J. Han, P. Mantas, and A. Senos, "Sintering kinetics of undoped and Mn-doped zinc oxide in the intermediate stage," *Journal of the American Ceramic Society,* 88[7] 1773-78 (2005).

149. D. Dollimore and P. Spooner, "Sintering studies on zinc oxide," *Transactions of the Faraday Society,* 67[] 2750-59 (1971).

150. T. Senda and R. C. Bradt, "Grain growth in sintered ZnO and ZnO-Bi_2O_3 ceramics," *Journal of the American Ceramic Society,* 73[1] 106-14 (1990).

151. T. Gupta and R. Coble, "Sintering of ZnO: I, Densification and grain growth," *Journal of the American Ceramic Society,* 51[9] 521-25 (1968).

152. T. Gupta and R. Coble, "Sintering of ZnO: II, density decrease and pore growth during the final stage of the process," *Journal of the American Ceramic Society,* 51[9] 525-28 (1968).

153. E. Secco, "Decomposition of zinc oxide," *Canadian Journal of Chemistry,* 38[4] 596-601 (1960).

154. D. R. Stull, "Vapor pressure of pure substances. Organic and inorganic compounds," *Industrial & Engineering Chemistry,* 39[4] 517-40 (1947).

155. H.-F. Ju, K. Ning, and K. Lu, "Roughening and destructive effects of sintering on micron-sized ZnO features," *Acta Materialia*, 141: 352-359 (2017).

156. L. Ding, R. L. Davidchack, and J. Pan, "A molecular dynamics study of sintering between nanoparticles," *Computational Materials Science,* 45[2] 247-56 (2009).

157. S. Kawashima, "Influence of ZnO evaporation on microwave dielectric loss and sinterability of Ba ($Zn_{1/3}Ta_{2/3}$) O_3 ceramics," *American Ceramic Society Bulletin,* 72[5] 120-26 (1993).

158. R. German and Z. Munir, "Surface area reduction during isothermal sintering," *Journal of the American Ceramic Society,* 59[9-10] 379-83 (1976).

159. D. F. Anthrop and A. W. Searcy, "Sublimation and thermodynamic properties of zinc oxide," *The Journal of Physical Chemistry,* 68[8] 2335-42 (1964).

160. H.-F. Ju, K. Ning, and K. Lu, "Centrifuge-aided micromolding of micron-and submicron-sized patterns," *Journal of the European Ceramic Society*, 38[2]: 637-645 (2018).

161. S. D. Shin, C. S. Sone, J. H. Han, and D. Y. Kim, "Effect of sintering atmosphere on the densification and abnormal grain growth of ZnO," *Journal of the American Ceramic Society,* 79[2] 565-67 (1996).

162. F. Oba, M. Choi, A. Togo, and I. Tanaka, "Point defects in ZnO: an approach from first principles," *Science and Technology of Advanced Materials,* 12[3] 1-14 (2011).

163. J. L. Zhao, W. Q. Zhang, X. M. Li, J. W. Feng, and X. Shi, "Convergence of the formation energies of intrinsic point defects in wurtzite ZnO: first-principles study by projector augmented wave method," *Journal of Physics: Condensed Matter,* 18[5] 1495-508 (2006).

164. P. L. Chen and I. W. Chen, "Grain boundary mobility in Y_2O_3: Defect mechanism and dopant effects," *Journal of the American Ceramic Society,* 79[7] 1801-09 (1996).

165. T. Titze, A. Lauerer, L. Heinke, C. Chmelik, N. E. Zimmermann, F. J. Keil, D. M. Ruthven, and J. Kärger, "Transport in nanoporous materials including MOFs: The applicability of Fick's laws," *Angewandte Chemie International Edition,* 54[48] 14580-83 (2015).

166. J. Vieira and R. Brook, "Kinetics of hot-pressing: The semilogarithmic law," *Journal of the American Ceramic Society,* 67[4] 245-49 (1984).

167. J. M. Carlsson, B. Hellsing, H. S. Domingos and P. D. Bristowe, "Electronic properties of a grain boundary in Sb-doped ZnO," *Journal of Physics: Condensed Matter*, 13[44] 9937-43 (2001).